J. Fluid Mech. (2024), *vol*. 999, A66, doi:10.1017/jfm.2024.641

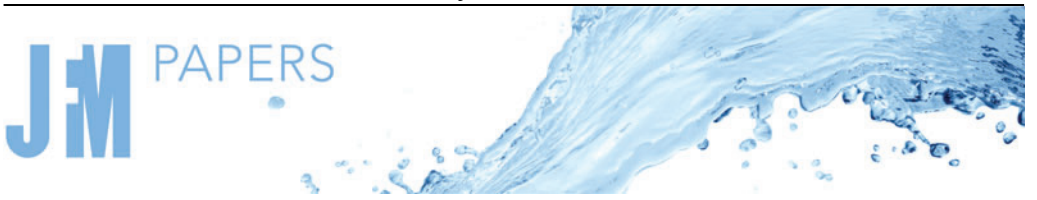

Aerodynamic heating in hypersonic shock wave and turbulent boundary layer interaction

Zhenyuan Tang[1], **Haonan Xu**[1], **Xueying Li**[1,†] **and Jing Ren**[1]

[1]Department of Energy and Power Engineering, Tsinghua University, Beijing, PR China

(Received 1 March 2023; revised 12 May 2024; accepted 4 August 2024)

In hypersonic flight the shock wave and turbulent boundary layer interaction (STBLI) sharply increases wall heat transfer that intensifies the aerodynamic heating problems. In this work the STBLI is modelled by compression ramp flow with a Mach number of 5, a Reynolds number based on momentum thickness of 4652 and a wall to recovery temperature ratio of 0.5. The aerodynamic heat generation and transport mechanisms are investigated in the interaction based on theoretical analysis and direct numerical simulation (DNS) that agrees with previous studies. A prediction correlation of wall heat flux in STBLI is deduced theoretically and validated by some representative data including the present DNS, which improves the prediction accuracy and can be applied to a wider *Ma* range compared with the canonical Q-P theory. The correlation indicates that the sharp increase of wall heat transfer in the STBLI can be explained by the boundary layer compression and the convection transport enhancement. Based on the DNS results, the aerodynamic heat generation and transport mechanisms are revealed in the separation, recirculation and reattachment zones in the STBLI. From this perspective, the peak heat flux can be further explained by the enhancement of near-wall turbulent energy dissipation, compression aerodynamic heat generation and the near-wall turbulent transport. The generation and transport of compression aerodynamic heat reveal the underlying mechanism of the strong correlation between the peak heat flux ratios and the pressure ratios in STBLIs.

Key words: hypersonic flow, turbulent boundary layers, shock waves

1. Introduction

The aerodynamic heating problem, known as the 'thermal barrier' (van Driest 1956), is a great challenge that aircraft face after reaching hypersonic speeds. The hypersonic turbulent boundary layer results in more serious aerodynamic heating than the laminar boundary layer and transitional boundary layer can even exceed that of fully laminar or

† Email address for correspondence: li_xy@tsinghua.edu.cn

turbulent flows (Longo 2003). When there is a shock interaction, the situation worsens because the shock further causes a sharp increase and an extreme peak of the wall heat transfer (Dolling 2001). Therefore, a comprehensive understanding of aerodynamic heating in hypersonic shock wave and turbulent boundary layer interactions (STBLIs) is of great importance for hypersonic thermal protection designs and the understanding of transitional SBLIs.

The heat transfer in a supersonic and hypersonic turbulent boundary layer has been well understood up to now (Huang, Lian & Choudhari 2022; Tong *et al.* 2022*a*) but it is still tricky to understand STBLIs. The Walz relation (Walz & Oser 1969) and Reynolds analogy describe the relation between the velocity and temperature field in the turbulent boundary layer, which also provide a way to predict the heat transfer coefficient (Eckert 1960; White & Majdalani 2006). The Walz relation has been validated in many studies for different wall temperatures from cold to hot (Pirozzoli, Grasso & Gatski 2004; Duan, Beekman & Martin 2010), different Mach numbers from supersonic to hypersonic (Duan, Beekman & Martin 2011) and many other operating conditions. As for temperature fluctuation, Morkovin proposed a strong Reynolds analogy (Morkovin 1962) that stated that the temperature fluctuation is negatively correlated with the velocity fluctuation. However, the strong Reynolds analogy shows obvious deviation in some cases and has been continually corrected in later research (Gaviglio 1987; Rubesin 1990; Huang, Coleman & Bradshaw 1995; Cebeci 2012). The above analogies are simple and graceful but unfortunately complicated changes will occur when turbulent boundary layers interact with shock waves.

The shock-induced adverse pressure gradient propagates upstream in the subsonic layer at the bottom of the turbulent boundary layer, which leads to the thickening of the boundary layer and even more complicated flow phenomena such as separation and reattachment as shown in figure 1. More details can be found by the representative filtered Rayleigh scattered images of hypersonic STBLIs given by Bookey *et al.* (2005). Many studies for supersonic conditions have shown that there is low-frequency 'breathing' movement in the separation bubble that leads to low-frequency oscillation of the separation shock wave. Previous experiments have found that in pressure power spectra there exist low-frequency fluctuations around separation points with a frequency of 1–2 orders of magnitude lower than the turbulence (Erengil & Dolling 1991), which is difficult to explain by the known turbulent coherent structures. Many explanations have been proposed to reveal the mechanisms of the low-frequency fluctuation, which can be classified into upstream mechanisms mainly attributing the phenomenon to the low-frequency large-scale burst events in the upstream turbulent boundary layer (Andreopoulos, Agui & Briassulis 1987, 2000; Erengil & Dolling 1993; Ganapathisubramani, Clemenn & Dolling 2007; Humble *et al.* 2009), and downstream mechanisms mainly attributing the phenomenon to the inherently unsteady flow structures in separation bubbles (Thomas, Putnam & Chu 1994; Wu & Martin 2008; Piponniau *et al.* 2009; Li *et al.* 2010; Priebe & Martin 2012). The mainstream view in current studies is that the upstream/downstream mechanisms always exist in STBLIs and, for a strong separation, the downstream mechanism is dominant while, for weak separation, both mechanisms are important (Clemens & Narayanaswamy 2014; Gaitonde 2015; Fan *et al.* 2022). Unlike pressure fluctuations, there is little data on aerodynamic heat fluctuations (Dolling 2001). Only some studies (Hayashi, Aso & Tan 1989; Bernardini *et al.* 2016) found that the wall heat flux is also intermittent while the heat flux results of Tong *et al.* (2022*b*) did not show clear low frequency. Moreover, the turbulent fluctuations are significantly amplified and turbulence behaviour is also significantly changed in STBLIs (Schreyer *et al.* 2018; Fang *et al.* 2020). Influenced by

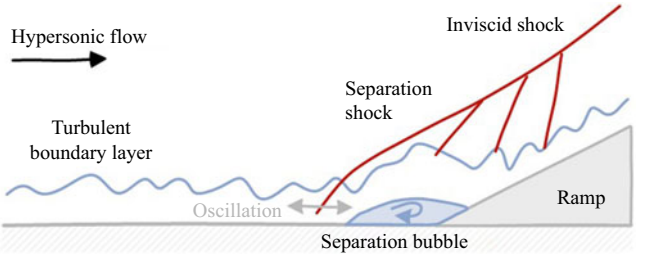

Figure 1. Schematic diagram of hypersonic STBLI flow field.

the above changes, the heat transfer in STBLIs becomes very complex and relevant public literature is very limited, especially for hypersonic conditions.

Limited research has provided wall heat flux distribution in a hypersonic STBLI region and further related the heat transfer to the pressure. The experiments of Delery & Coet (1991) showed that separation occurred in STBLIs and the wall heat flux sharply increased downstream. They pointed out that the increase of heat transfer was because the shear layer detached and large vortices developed that promoted the heat exchange between near-wall fluids and external high enthalpy flow. The experiments of Coleman & Stollery (1972) indicated that the wall heat flux can achieve more than 30 times that in incoming undisturbed boundary layers, even beyond the heat flux at stagnation points. Holden (1972, 1977) systematically measured the wall heat flux both in hypersonic compression corner flows and shock impingement flows for different incoming boundary layer states, the Reynolds number, the Mach number and the shock strength with focus on the initial separation. Schülein, Krogmann & Stanewsky (1996) conducted a series of experiments of two-dimensional (2-D) hypersonic impinging STBLIs at a Mach number of 5 for shock generator angles of 6°, 10° and 14°, which provided precious records of the surface quantity and mean flow boundary layer profiles in hypersonic STBLIs. The numerical investigation at different Mach numbers (Babinsky & Harvey 2011) has also confirmed that the heat transfer rises rapidly in STBLIs and the peak wall heat fluxes strongly depend on the Mach number. Recent studies (Bernardini *et al.* 2016; Wagner *et al.* 2017; Zuo 2023) pointed out that wall temperatures greatly influence the separation and wall heat flux in STBLIs. Due to the separation, the Reynolds analogy is no longer valid in STBLIs as proved by the measurements such as the results measured by the infrared thermography and oil film interference of Schülein (2006). Therefore, other prediction methods were developed. Markarian (1968) collated some measurement results at that time and proposed a widely used correlation (denoted by QP85): $\dot{q}_{max}/\dot{q}_u = (p_{max}/p_u)^{0.85}$, where the subscript u represents the reference values upstream where boundary layers are undisturbed. Later, Back & Cuffel (1970) proved this power relation theoretically and Holden (1972, 1977) proved it experimentally. However, the exponent in the correlation was put to 0.8 by Hung & Barnett (1973). Coleman & Stollery (1972) deduced a more elaborate Q-P relation based on the reference enthalpy and shock wave relation, which was validated in their gun wind tunnel experiments at a Ma of 9. Recently, Murray, Hillier & Williams (2013) validated the QP85 theory also in the Ma 9 wind tunnel at Imperial College. However, the direct numerical simulation (DNS) results of Priebe & Martín (2021) and Tong *et al.* (2022*b*) showed some discrepancy with the QP85 prediction and the large-eddy simulation results of Helm & Martín (2022) showed obvious deviation with QP85 prediction. Recent numerical investigations have further shown that the exponent of the power law is dependent on the wall temperature and mainstream Mach number. Volpiani, Bernardini & Larsson (2020) pointed out that the exponent is 0.75 for cold wall

conditions while 0.85 for hot wall conditions based on their DNS results. Zuo (2023) pointed out that the exponent may range from 0.75 to 0.95 based on their RANS results. Above all, the wall heat flux in hypersonic STBLIs is not understood well and needs further study.

The above progress on the wall heat transfer prediction in STBLIs is not easy to achieve but is of great significance; nevertheless, it does not reveal the relationship between wall heat fluxes and the aerodynamic heat generation and transport that are important for wall heat transfer control. Recently, Tong *et al.* (2022*b*) used the wall heat flux decomposition proposed by Sun *et al.* (2021) to investigate the mechanisms of heat transfer in STBLIs at a Ma of 2.25 and the quantitative analysis showed that the terms related to Reynolds stress and turbulent transport had the greatest influence on the wall heat transfer. The wall heat flux decomposition provides a clever method and some original insights to understand the aerodynamic heat. However, the method is based on the total energy equation that couples the kinetic energy transport and transformation resulting in some cumbersome and unclear terms in the decomposition formula. Besides, the conservation of the equation hides the energy dissipation that is an important mechanism of the aerodynamic heating. As for three-dimensional (3-D) STBLIs such as swept interactions, which are hotspots in the current research, aerodynamic heating analyses are also lacking though many studies (Adler & Gaitonde 2019; Vanstone & Clemens 2019; Padmanabhan *et al.* 2021) have investigated the applicability of flow field analyses in 2-D STBLIs to 3-D cases. Therefore, aerodynamic heating analyses are of significance and require directly conducted from the heat transport equation to reveal the aerodynamic heat generation and transport mechanisms in STBLI.

In summary, the research and data of hypersonic STBLIs are rather limited, not to mention the prediction or understanding of the wall heat transfer. Hence, the main purpose of this paper is to systematically investigate aerodynamic heating in hypersonic STBLIs by theoretical analysis and DNS. In this paper a prediction correlation of wall heat flux in STBLIs is proposed based on the boundary layer thickness and preliminarily confirmed by some representative data including the present DNS results. To explain the mechanisms of the wall heat flux increase, the paper further analyses the aerodynamic heat generation and near-wall transport based on DNS statistics results of the terms in the heat transport equation.

The paper is organized as follows. The DNS method and validation are described and the basic flow structures in STBLIs are introduced in § 2. The wall heat transfer in STBLIs is analysed theoretically and the heat transport equation is given in § 3. Based on these theories, aerodynamic heating in the STBLI is investigated including the mean wall heat flux increase and aerodynamic heat generation with near-wall transport in § 4. Finally, conclusions are summarized in § 5.

2. The DNS method

The STBLI model is introduced with the governing equations and boundary conditions in this section. Direct numerical simulation is used to solve the problem and some important details are provided including the turbulence generation method, numerical schemes and computational grid. Finally, the DNS results are carefully validated by comparing with previous results and theories of hypersonic turbulent boundary layers and interaction regions.

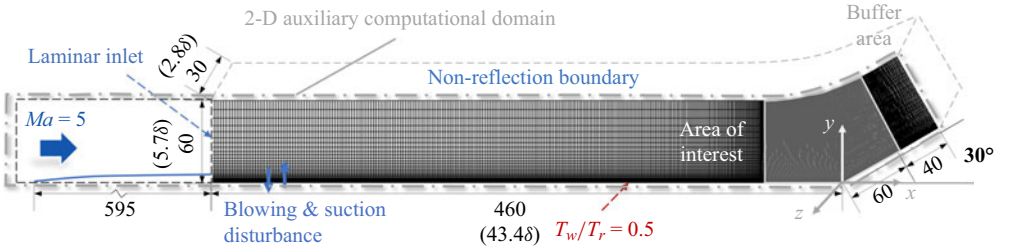

Figure 2. Computational domain and boundary condition of ramp flow (unit: mm).

Boundary condition	Ma	Re (per 1 mm)	T_∞ (K)	T_w/T_∞	T_w/T_r
	5.0	7980	221	2.72	0.5
Boundary layer	δ (mm)	θ (mm)	δ_v (mm)	Re_τ	Re_θ
	10.6	0.58	0.015	700	4652

Table 1. Key parameters of boundary condition and boundary layer at the reference position ($x = -60$ mm).

2.1. *Computational model and set-up*

The compression ramp flow is used to model the STBLI and the geometry and size are shown in figure 2. The 2-D auxiliary computational domain framed by a grey dotted line is used by an auxiliary flow simulation for providing the laminar inlet boundary condition and the initial value for the 3-D principal computational domain covered by the computational grid. The STBLI in the corner is the area of interest in the paper. The outlet extends a buffer area with a sparse grid to dissipate the disturbance reflected from the outlet. A Cartesian coordinate system is established with the origin set at the corner vertex, x in the streamwise direction, y in the wall-normal direction and z in the spanwise direction.

The governing equations are Navier–Stokes equations in the curvilinear coordinate system as

$$\frac{\partial \boldsymbol{U}}{\partial t} + \frac{\partial (\boldsymbol{F_i} + \boldsymbol{F_{v,i}})}{\partial \xi_i} = 0, \tag{2.1}$$

where $\boldsymbol{U}$ is the conserved variable, $\boldsymbol{F_i}$ is the inviscid flux and $\boldsymbol{F_{v,i}}$ is the viscous flux (see (Fu, Ma & Li 2010) for detailed expressions). Besides, the viscous stress is modelled by the Newtonian fluid, the viscosity of which is calculated by the Sutherland formula. The heat flux is modelled by Fourier's law and the thermal conductivity is calculated from the viscosity and Prandtl number of 0.7. As for the state equation, the ideal gas model is used with the specific ratio equal to 1.4. No turbulence model is used and the above equations are closed.

The main boundary conditions are described in figure 2 and listed in detail in table 1. The inlet is a laminar profile extracted from a 2-D simulation and the outlet is a supersonic outflow. The blowing and suction disturbance is introduced from $x = -440$ to -410 mm to force the boundary layer into the transition to generate turbulence. The specific form of the disturbance is the same as Pirozzoli *et al.* (2004) and cited as

$$v_{bs}(x, z, t) = AU_\infty f(x) g(z) h(t), \tag{2.2}$$

where in the present paper the intensity of the disturbance is set as $A = 0.2$, and $f(x)$, $g(z)$ and $h(t)$ are defined as

$$\left.\begin{aligned} f(x) &= \frac{4}{\sqrt{27}}\sin\theta_x(1-\cos\theta_x), \quad \theta_x = 2\pi\frac{x-x_a}{x_b-x_a}, \\ g(z) &= \sum_{n=1}^{3}\frac{0.8^{n-1}}{\sum_{n=1}^{3}0.8^{n-1}}\sin\left(2\pi n(z/L_z+\phi_n)\right), \\ h(t) &= \sum_{m=1}^{5}\frac{0.8^{m-1}}{\sum_{m=1}^{5}0.8^{m-1}}\sin\left(2\pi m(\beta t+\phi_m)\right), \end{aligned}\right\} \tag{2.3}$$

where the basic disturbance frequency $\beta = 0.32U_\infty/\delta_d$ or $1.24U_\infty/\delta$, where δ_d is the nominal thickness of the laminar boundary layer at the disturbance location while δ is the nominal thickness of the turbulent boundary layer at the reference location ($x = -60$ mm). The phase parameters, ϕ_n and ϕ_m, are random numbers ranging from 0 to 1. According to the above form, the disturbance flow rate is zero on average. Ignoring the rarefied gas effect, no slip wall assumption is reasonable and applied to the wall condition of the velocity field. Considering the actual wall situations in flights, a cold wall condition is applied in the simulation. The isothermal bottom wall is used with $T_w/T_r = 0.5$, where T_r is the recovery temperature calculated by recovery coefficient $r = Pr^{1/3}$. The top boundary is non-reflective. The spanwise boundary condition is periodic.

To describe the incoming turbulent boundary layer quantitatively, some characteristic thicknesses at the reference location are also listed in the second line of table 1. Here δ is the nominal thickness, θ is the momentum thickness and δ_v is the viscous scale on the wall. Based on these thicknesses, the corresponding Reynolds number at the reference location can be obtained and are $Re_\delta = \rho_\infty U_\infty\delta/\mu_\infty = 8.46\times10^4$, $Re_\theta = \rho_\infty U_\infty\theta/\mu_\infty = 4652$ and $Re_\tau = \rho_w u_\tau\delta/\mu_w = \delta/\delta_v = 700$. Note that δ and δ_v will be used to non-dimensionalize length quantities later.

In the present DNS, a finite difference method is used on the structured grid. The inviscid flux terms in (2.1) are split by the Steger–Warming flux vector splitting method and then solved by a hybrid scheme that is composed of a seventh-order low dissipation upwind scheme in the smooth region, a seventh-order WENO scheme in the non-smooth region and a fifth-order WENO scheme in the extremely non-smooth region. The smoothness of the flow field is given by a modified Jameson shock sensor (Jameson, Schmidt & Turkel 1981). The viscous terms are solved by a sixth-order central difference scheme. To ensure the numerical accuracy at the boundary, virtual grid points are extrapolated from inner grid points. Time advance is solved by the third-order Runge–Kutta scheme and 153 000 time steps or $92\delta/U_\infty$ are calculated during the sampling stage with sampling every 40 steps. The statistical results of the skin friction, the wall heat flux and the incoming turbulent boundary layer profiles all indicate that the sampling time is statistically convergent. The computational grid is an important factor of the DNS and will be introduced specially in the next subsection. The above calculation is performed on the open source code OpenCFD-SC, which has been widely used and validated by the development team in DNS of compressible turbulence (Li *et al.* 2010; Liang *et al.* 2012; Tong *et al.* 2018; Tong, Duan & Li 2021; Tong *et al.* 2022*b*).

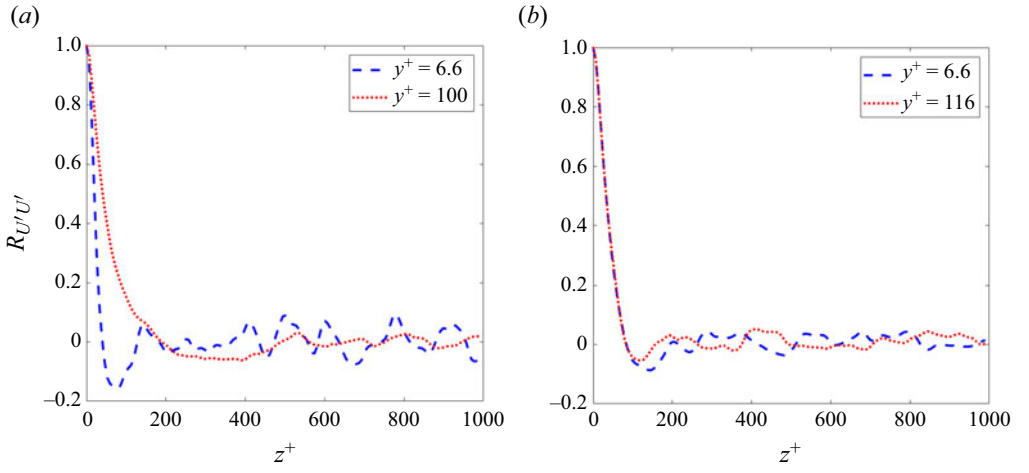

Figure 3. Spanwise two-point correlations of the fluctuating velocity at (*a*) $x = -60$ mm and (*b*) $x = 0$ mm.

2.2. *Computational grid*

The DNS grid is required to solve turbulence at all scales and, hence, the computational grid needs to be designed and examined carefully. As shown in figure 2, the present grid in the streamwise direction is refined near the corner. The streamwise grid in the upstream turbulent boundary layer ($x < -60$ mm) is refined by a three order function from inlet grid scale to corner grid scale and the streamwise grid in the corner area ($x > -60$ mm) is kept uniform, as indicated in grey in the figure. The near-wall grid is stretched with the geometric form of $y_j = \Delta y_1(\alpha^{j-1} - 1)/(\alpha - 1)$, where Δy_1 is the first grid height near the wall and α is the stretching rate and set to 1.0293 here. In the spanwise direction the grid distributes uniformly. The total grid number is $N_x \times N_y \times N_z = 2660 \times 204 \times 300 = 1.63 \times 10^8$. Dimensionless by the viscous scale δ_v, the first layer grid height is $y^+ = 0.33$ at the reference station and is $y^+ = 0.59$ at its maximum point on the ramp. The near-wall first layer grid scale is also on the same order with the turbulence dissipation scale considering the Kolmogorov dissipation scale, $\eta/\Delta y_1 = 1.04$, which is estimated by the method of Zhang *et al.* (2017). The streamwise grid scale is $\Delta x^+ = 6.6$ in the interaction area, $\Delta x^+ = 6.6$–17.5 in the upstream turbulent boundary layer and in the spanwise grid scale is $\Delta z^+ = 6.6$, which are dimensionless by the reference viscous scale. The spanwise scale of the computational domain should solve the largest vortices, which is proved by the spanwise two-point correlation. The results indicate that with the distance increasing, the correlations decay rapidly to near 0 both at the inlet and the corner station, as shown in figure 3. In the near-wall region ($y^+ = 6.6$) the correlation shows small fluctuations due to the streak-like coherent structures. The above scale analysis preliminarily suggests that the present grid can be applied to solve the near-wall turbulence.

Furthermore, turbulent energy spectra also show a good resolution of small turbulence scales. As shown in figure 4, the near-wall turbulent energy spectra at the inlet and the corner both present three characteristic regions: the inertial region with a peak, the inertial sub-region showing typical $-5/3$ power law and the dissipation region where the energy decays faster with increasing wavenumber. In the incoming turbulent boundary layer (figure 4*a*), with the distance from the wall increasing, the peak wavenumber decreases, which indicates the energetic scale becomes larger, or quantitatively from $L_z/15$ near the

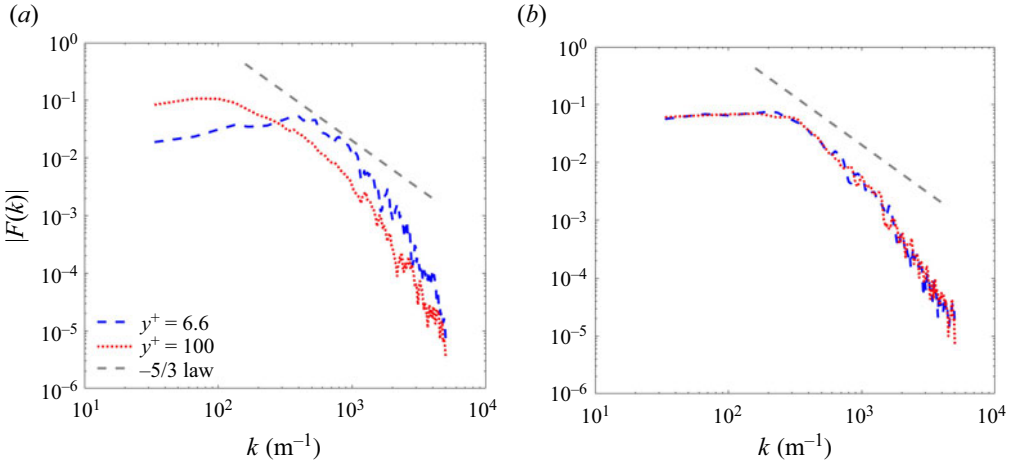

Figure 4. Near-wall turbulent energy spectra at the inlet and the corner at (*a*) $x = -60$ mm and (*b*) $x = 0$ mm.

wall to $L_z/3$ far from the wall where L_z is the spanwise length of the computational domain. However, around the corner (figure 4*b*), the spectra almost remain the same at a different distance from the wall, which indicates that the turbulence is more uniform in the corner region. The above results are consistent with the existing knowledge and prove that the present grid covers the small turbulent scale and is capable of solving the turbulence.

The most convincing and direct method to prove the DNS grid resolution is the grid convergence study; see table 2 for the five different grid set-ups used in this work. Case M3 is the grid introduced at the beginning of the subsection. Here N_x, N_y, N_z are grid numbers in the streamwise, wall-normal and spanwise directions and the total grid number of these cases is from 1.25×10^8–2.44×10^8. In cases M1–M4, only the wall-normal grid is changed by changing the first grid height and maintaining the stretching rate, with y^+ ranging from 1.31–0.16 at the reference station and y^+ ranging from 2.08–0.30 at the maximum point that is in the interaction area. The wall-normal grid scale at the edge of the boundary layer ranges from 18.0–16.6 at the reference station, which is similar to previous literature on STBLIs (for example, Δy_e^+ is 15.0 in Zhu *et al.* (2017) and 23.0 in Tong *et al.* 2018). The wall-normal grid scale in the shear layer above the separation bubble is normalized by local viscous scale, that is, $\Delta y_{sl}^* = \Delta y/(\sqrt{\nu_{sl}/(\partial u/\partial y)_{sl}})$, where ν_{sl} and $(\partial u/\partial y)_{sl}$ mean the local values on the zero velocity line in the shear layer. Here Δy_{sl}^* at $x = 0$ mm are all less than 1 for the five cases. The wall-normal grid Reynolds number is also given, which is defined as $Re_{\Delta_n} = \rho_w U_\infty \Delta_n/\mu_w$, where Δ_n is equal to Δy_1 in the paper. Previous studies of aerodynamic heating over blunt bodies show that the calculation reaches grid convergent generally at Re_{Δ_n} of around 10 and, for low-dissipation numerical schemes, the value can be relaxed to 40 (Ma & Liu 2023). Here Δx^+ ranges from 6.6 to 17.5 for all cases, which is reasonable according to Georgiadis, Rizzetta & Fureby (2010) who suggest Δx^+ should be 10–20 for DNS. As for case M5, the spanwise grid is refined based on case M3, with z^+ from 6.6 to 4.4 while the same grid is used for the other two directions. The final results of the grid convergence test are shown in figure 5. The results show that for the incoming turbulent boundary layer, *St* is basically unchanged with the increase of grid number. For the peak location, the peak *St* increases with the increase

Case	$N_x \times N_y \times N_z$	Δx^+	y^+_{ref}	y^+_{max}	Δy^+_e	Δy^*_{sl}	Δz^+	α	Re_{Δ_n}
M1	2660 × 157 × 300	6.6–17.5	1.31	2.08	18.0	0.77	6.6	1.0292	28
M2	2660 × 180 × 300	6.6–17.5	0.66	1.15	17.8	0.52	6.6	1.0293	14
M3	2660 × 204 × 300	6.6–17.5	0.33	0.59	17.2	0.38	6.6	1.0293	7
M4	2660 × 227 × 300	6.6–17.5	0.16	0.30	16.6	0.32	6.6	1.0295	4
M5	2660 × 204 × 450	6.6–17.5	0.33	0.60	17.2	0.38	4.4	1.0293	7

Table 2. Grid set-up for the grid convergence test.

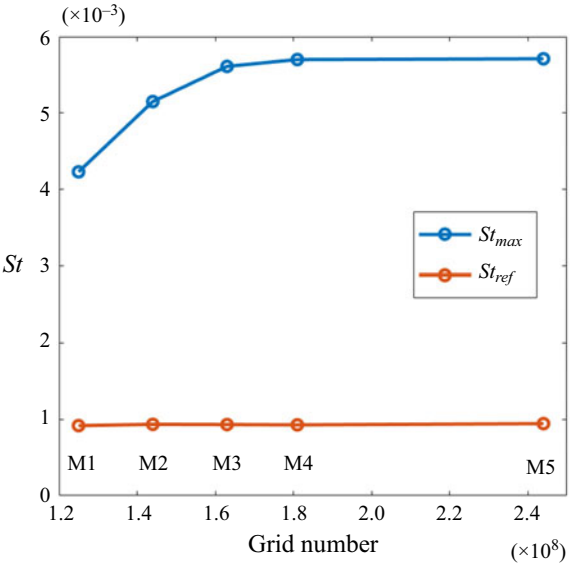

Figure 5. The Stanton number at the reference position and at the maximum position for the varying grid sizes.

of the grid number until the grid size reaches that of case M3, which indicates the grid convergence is basically reached for case M3.

Given that the paper focuses on the near-wall aerodynamic heating, the wall-normal grid convergence is investigated in detail and the results of the corresponding cases M1–M4 are shown in figure 6. According to the skin friction results (figure 6*a*), it can be found that with the refinement of the near-wall grid, the flow transition is slightly advanced. For all cases in the current test, the results of the incoming turbulent boundary layer are almost the same. With the refinement of the near-wall grid, the separation point is basically unchanged but the reattachment point is advanced and then the downstream friction coefficient increases until case M3 reaches the grid convergence of the flow field. As for heat transfer (figure 6*b*), the results of the incoming turbulent boundary layer are also basically consistent for all cases, which indicates that incoming flow has been well solved. With the near-wall grid refinement, the downstream heat transfer coefficient increases and M3 also achieves grid convergence of the heat transfer simulation. Moreover, as expected, the pressure results are not sensitive to changes of the wall-normal grid as shown in figure 6(*c*).

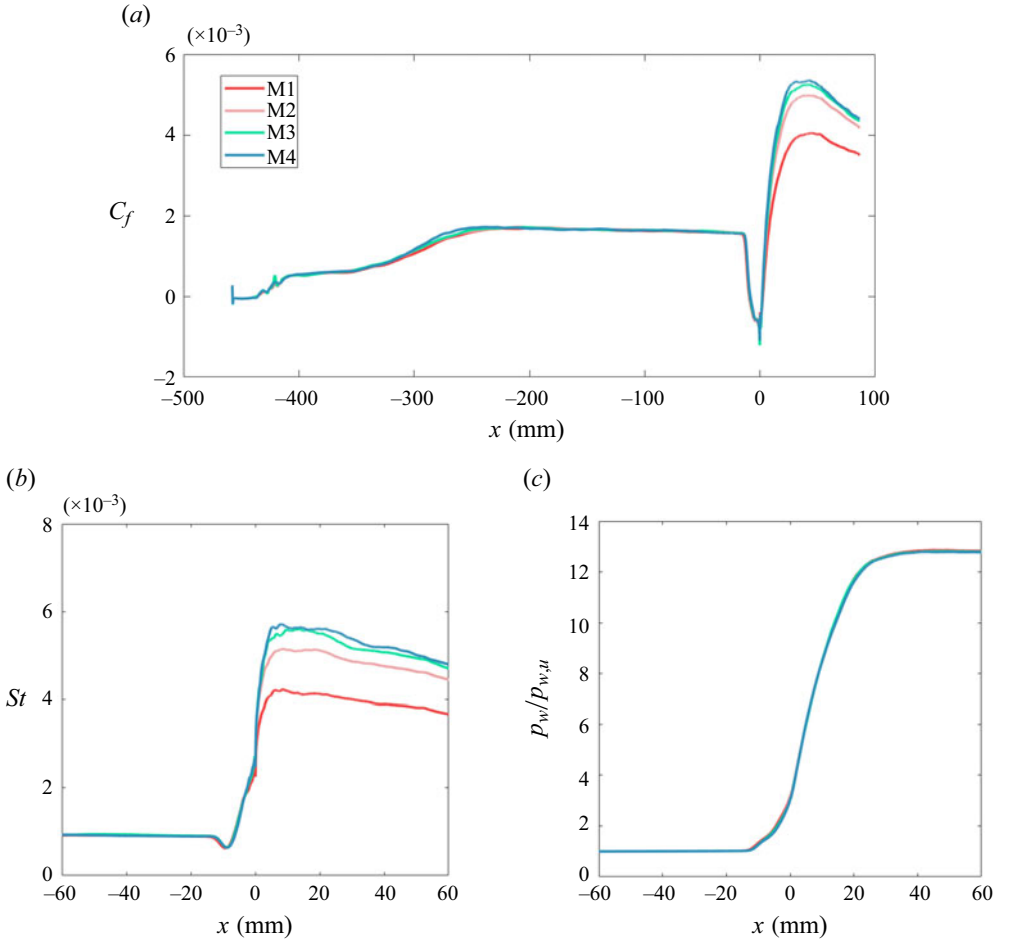

Figure 6. (*a*) Skin friction coefficients, (*b*) the Stanton number and (*c*) wall pressure ratio distribution along the streamwise direction for the cases of varying wall-normal grid sizes.

The spanwise grid convergence details are shown in figure 7. For heat transfer, as shown in figure 7(*a*), with the refinement of the spanwise grid, the *St* before the peak point and the peak *St* remain unchanged but the *St* after the peak point increases slightly, showing that grid convergence is essentially achieved for the present study. For the pressure ratio, as shown in figure 7(*b*), the results are also almost identical between the cases of different spanwise grids.

Furthermore, the grid convergence of some representative higher-order statistics are examined carefully as shown by the root mean square (r.m.s.) of streamwise turbulent velocity in figure 8 and the wall-normal turbulent scalar flux in figure 9. In the undisturbed boundary layer ($x = -60$ mm) there is no significant difference in the u_{rms} profiles among the five different grids listed in table 2. However, as the boundary layer is interacted by the shock, the required grid resolution increases. In the near-wall region the r.m.s. of the streamwise turbulent velocity for cases M1 and M2 is slightly higher until case M3 achieves grid convergence in the separation bubble region ($x = 0$ mm) and downstream boundary layer ($x = 60$ mm), as shown in figure 8(*b*,*c*). The turbulent scalar flux profiles

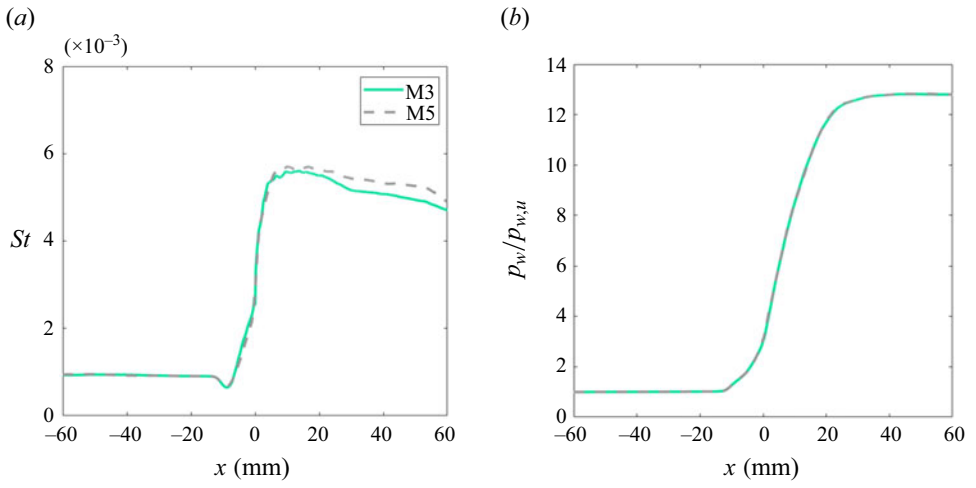

Figure 7. (*a*) The Stanton number and (*b*) wall pressure ratio distribution along streamwise direction for the cases of varying spanwise grid sizes.

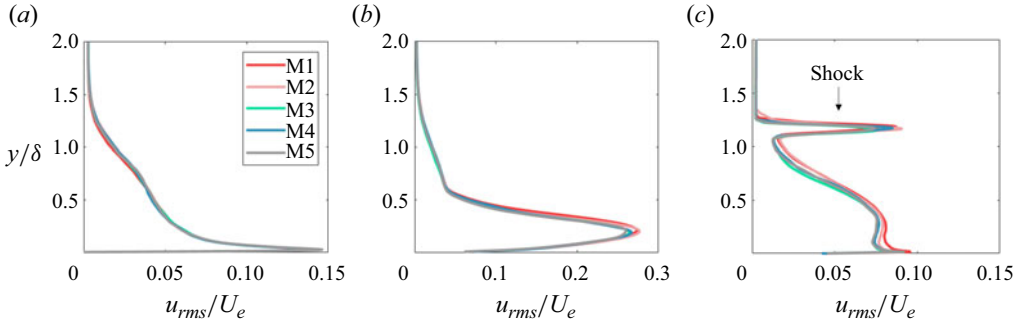

Figure 8. The r.m.s. of streamwise turbulent velocity profiles at the (*a*) upstream boundary layer ($x = -60$ mm), (*b*) separation bubble region ($x = 0$ mm) and (*c*) downstream boundary layer ($x = 60$ mm) for the cases of varying grid sizes.

show similar grid convergence as shown in figure 9. Compared with the wall gradients, the turbulence statistics profiles are less sensitive to the grid and show better grid convergence.

In summary, by careful analysis and validation, case M3 basically achieved grid convergence and can solve the small-scale turbulence near the wall. The results of case M3 are used to analyse the aerodynamic heating mechanisms in this work.

2.3. *Validation of the incoming turbulent boundary layer*

The turbulent boundary layer is generated by the forced transition with spatial development. Hence, in this section the development degree and the calculation accuracy are carefully checked for the skin friction distribution, velocity and temperature profile at the reference station $x_{ref} = -60$ mm. Note that the results in this paper are mostly average so the average symbol is omitted without confusion for the reason of simplification. The averaging operations in the present study are conducted in both time and spanwise direction.

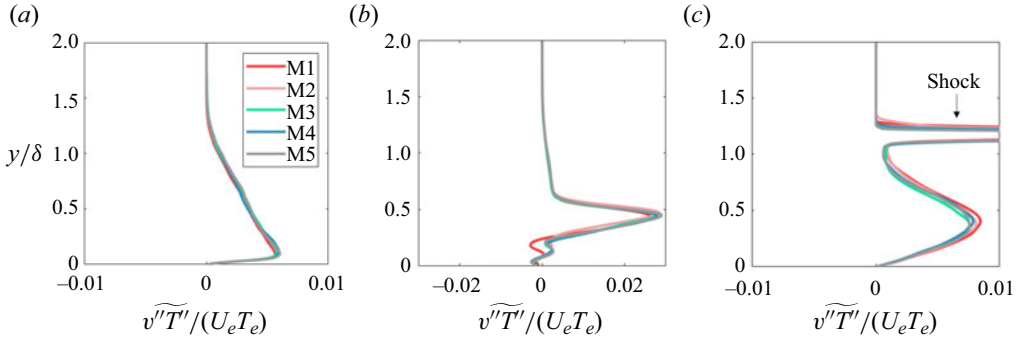

Figure 9. The wall-normal turbulent scalar flux profiles at the (*a*) upstream boundary layer ($x = -60$ mm), (*b*) separation bubble region ($x = 0$ mm) and (*c*) downstream boundary layer ($x = 60$ mm) for the cases of varying grid sizes.

The skin friction C_f describes the boundary layer development from the laminar flow to turbulence as shown in figure 10, which also provides the C_f prediction in laminar compressible boundary layers of Eckert (1955) and the prediction in turbulent compressible boundary layers of White & Majdalani (2006), which is also given as

$$C_f = 0.455 \Bigg/ \left[S \ln \left(\frac{0.06}{S} Re_x \frac{\mu_e}{\mu_w} \sqrt{\frac{T_e}{T_w}} \right) \right]^2, \quad S = \frac{(T_r/T_e - 1)^{1/2}}{\sin^{-1} A + \sin^{-1} B}, \tag{2.4a,b}$$

where

$$\left.\begin{aligned} A &= \frac{2a^2 - b}{(b^2 + 4a^2)^{1/2}}, \quad B = \frac{b}{(b^2 + 4a^2)^{1/2}}; \\ a &= \left(r \frac{\gamma - 1}{2} Ma_e^2 \frac{T_e}{T_w} \right)^{1/2}, \quad b = \frac{T_r}{T_w} - 1. \end{aligned}\right\} \tag{2.5}$$

In the prediction, the effective development origin of the turbulent boundary layer is hard to determine due to the uncertainty of the forced transition and, hence, it is simply set at the leading edge of the plate in the paper to provide a reference. In the inlet of the computational domain, C_f is around the laminar value. At $x > -400$ mm, C_f increases quickly, which indicates that the transition occurs while around $x = -250$ mm, C_f reaches a maximum value that indicates the transition is near completion. After $x = -150$ mm, C_f decreases slowly and steadily as predicted by the theory, which indicates the turbulence can be considered fully developed, that is to say, the turbulence is fully developed at the corner inlet ($x = -60$ mm).

The turbulent boundary layer profiles at the corner inlet are further validated and the sources of reference data are listed in table 3. Duan *et al.* (2010) and Chu, Zhuang & Lu (2013) provided DNS results of hypersonic turbulent boundary layers for similar conditions to this paper. The DNS results of Huang *et al.* (2022) and Zhang, Duan & Choudhari (2018) are also cited for later comparison and discussion. Spalart (1988) provided classical DNS results of incompressible turbulent boundary layers while Sillero, Jimenez & Moser (2013) provided recent DNS data of higher Reynolds numbers.

The mean velocity and temperature results at the reference station are compared with the previous DNS results and classic theories as shown in figure 11. The velocity profile

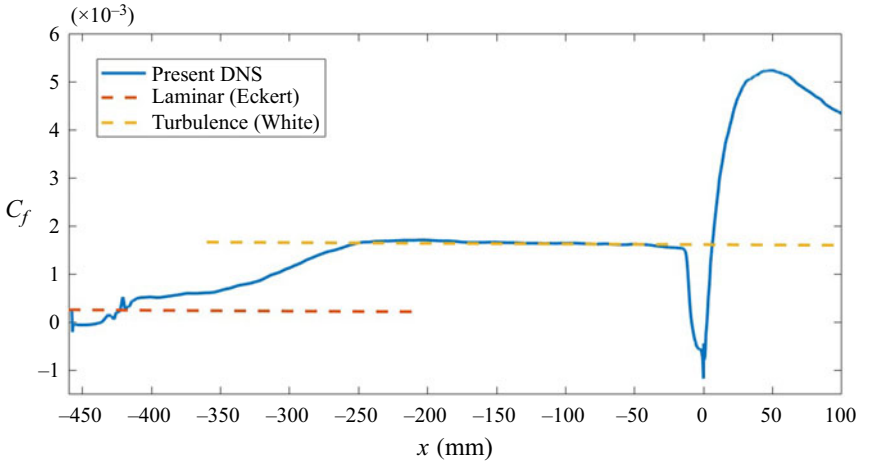

Figure 10. Turbulence development validation by comparing the skin friction coefficient with the values in laminar and turbulent boundary layer.

References	Ma	Re_θ	Re_τ	T_w/T_∞	T_w/T_r
Present DNS	5.0	4652	700	2.72	0.50
Duan *et al.* (2010)	4.97	3012	522	2.89	0.54
Chu *et al.* (2013)	4.9	3480	532	2.62	0.50
Huang *et al.* (2022)	4.9	14 800	774	4.79	0.91
Zhang *et al.* (2018)	5.84	2120	450	1.77	0.25
Spalart (1988)	0.0	1410	660	—	—
Sillero *et al.* (2013)	0.0	4080	1307	—	—

Table 3. Reference data with key incoming conditions for the hypersonic turbulent boundary layer validation.

in wall coordinates is shown in figure 11(*a*) after van Driest transformation defined as

$$U_{vd}^{+} = \int_0^{U^+} \sqrt{\rho/\rho_w}\,\mathrm{d}U^{+}. \tag{2.6}$$

The transformation collapses the profiles well to the classic incompressible wall law, showing linear law at $y^+ < 4$ and logarithmic law at $y^+ = 30$–200. Compared with the DNS results of Duan *et al.* (2010), there is no significant difference overall except for the wake layer. The slight deviation of up to 3 % can be attributed to the difference of the Reynolds number and the turbulence generation method (Wenzel *et al.* 2018). The accuracy of the velocity profile is considered enough for the current research.

The temperature–velocity relation profile is also a key result of the compressible turbulent boundary layer, which is shown in figure 11(*b*). Compared with the canonical Walz relation (Walz & Oser 1969),

$$\frac{T}{T_e} = \frac{T_w}{T_e} + \frac{T_r - T_w}{T_e}\frac{U}{U_e} + \frac{T_e - T_r}{T_e}\left(\frac{U}{U_e}\right)^2, \quad \frac{T_r}{T_e} = 1 + r\frac{\gamma - 1}{2}Ma_e^2, \tag{2.7a,b}$$

the present DNS also shows good consistency and indicates that the temperature presents a good quadratic relation with the velocity. The slight deviation in the middle part is because

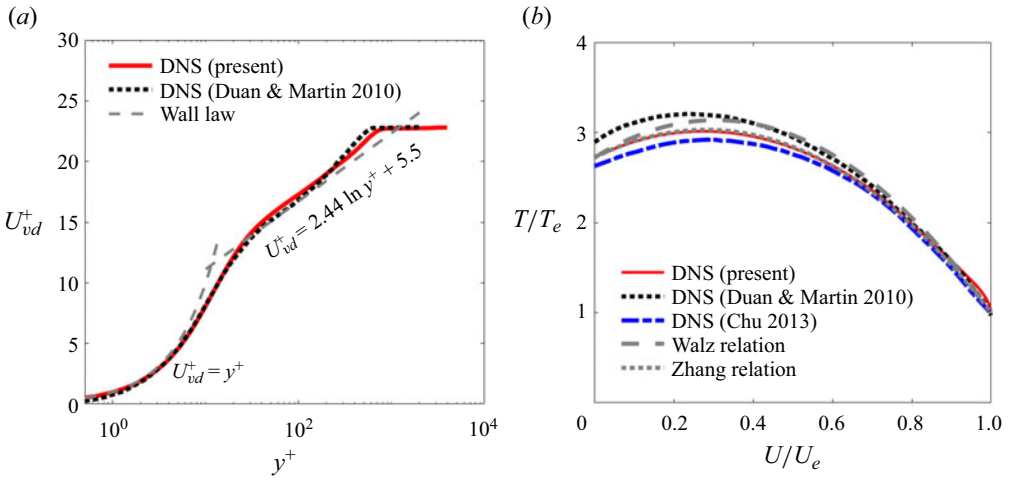

Figure 11. (*a*) Mean streamwise velocity profiles and (*b*) temperature–velocity relation of the turbulent boundary layer at the reference station.

the cold wall deviates from an assumption of the Walz relation, i.e. turbulent Prandtl number $Pr_t = 1$. Zhang *et al.* (2014) considered the wall heat flux effect and proposed a more generalized relation that just replaces r in (2.7) with

$$r_g = \frac{2(T_w/T_e - 1)}{(\gamma - 1)Ma_e^2} + 4Pr\frac{(T_r/T_e - T_w/T_e)}{(\gamma - 1)Ma_e^2}\frac{St}{C_f}. \tag{2.8}$$

The result of the Zhang relation shows good agreement with the present DNS. Compared with previous DNS results, there are some minor deviations mainly near the wall and the present DNS profile is closer to that of Chu *et al.* (2013), which is because the wall temperatures are slightly different for these cases and the wall temperature of the present DNS is closer to that of Chu *et al.* (2013). On the whole, the temperature results of the present DNS is accurate and reliable.

The r.m.s. profile of the fluctuating velocity provides more detail on the turbulent boundary layer as shown in figure 12. Good qualitative agreement is achieved compared with the previous DNS of Duan *et al.* (2010) and Chu *et al.* (2013) both in global coordinates and wall coordinates. The present DNS is also close to the results of Huang *et al.* (2022) for similar Ma and Re_τ, except the peak of Huang *et al.* (2022) is sharper near the wall. The deviation can be attributed to the wall temperature difference, which can be inferred from the comparison with DNS data for a lower wall temperature (Zhang *et al.* 2018). The profiles present a peak near the wall in the buffer region of the near-wall turbulence. At the edge of the boundary layer, the present DNS fluctuation is slightly higher than the reference data, which might be explained by the difference of the Reynolds number as listed in table 3. The relative deviation at the edge of the boundary layer is 5 % compared with data of Huang *et al.* (2022) for similar Re_τ, which is acceptable for the present study. The r.m.s. profile of the fluctuating velocity after Morkovin transformation also confirms the Morkovin's assumption, as shown in figure 12(*a*), that predicts that the profile will collapse to the incompressible boundary layer profile after the transformation. It can be seen from the results that in $y/\delta < 0.4$ the Morkovin's assumption is well validated while in $y/\delta > 0.4$ the DNS compressible results are all a little bit larger compared with classical data from Spalart (1988), which is also observed by Pirozzoli *et al.*

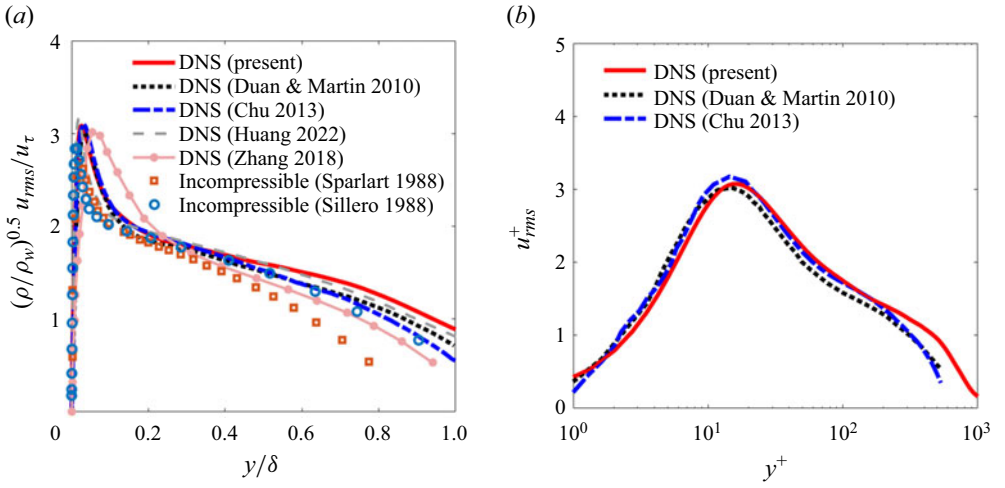

Figure 12. Root mean square of the fluctuating streamwise velocity of the turbulent boundary layer at reference station in (*a*) global coordinate and (*b*) wall coordinate.

(2004). Considering recent data for higher Reynolds number from Sillero *et al.* (2013), better consistency can be observed between compressible and incompressible boundary layers. On the whole, the r.m.s. profile of velocity fluctuation shows reasonable agreement with the previous turbulent boundary layer theories and results.

In summary, the compressible turbulent boundary layer at the corner inlet is fully developed and the present DNS results of the incoming turbulence including the flow field, temperature field and fluctuations are accurate and reliable enough for the current study.

2.4. *The flow results in the interaction region*

The STBLI results are validated from the flow field including the wave structure, pressure distribution and interaction length in this subsection and the flow field is also analysed preliminarily as the starting point of the aerodynamic heat analysis.

The shock wave structure of the present DNS is given in schlieren visualization in figure 13 with the previous experiment record of Li (2007), and also given in velocity field in figure 14. The shock structure in the compression ramp flow is qualitatively consistent with the experimental schlieren image as shown in figure 13 for similar Ma and the results both show that the hypersonic shock wave is deeply immersed in the boundary layer and obviously curved due to the interaction with the near-wall flow at the bottom. More details of the flow field are described in figure 14. The shock wave agrees well with the inviscid shock wave theory when far away from the corner. As for the turbulent boundary layer, it is compressed after passing through the shock wave and separates slightly at the bottom around the corner. The recirculation bubble lifts the shear layer leading to the enhancement of the momentum exchange between the bottom of the boundary layer and the mainstream so that the low velocity fluid can obtain momentum as the pressure rises. Since the separation area only occupies a very small part of the boundary layer, there is no clear reattachment shock wave in the flow field. Quantitatively, the boundary layer separates at $x_S = -8.66$ mm and reattaches at $x_R = 2.25$ mm on the ramp. Above all, the shock wave structure of the present DNS is qualitatively consistent with the previous study

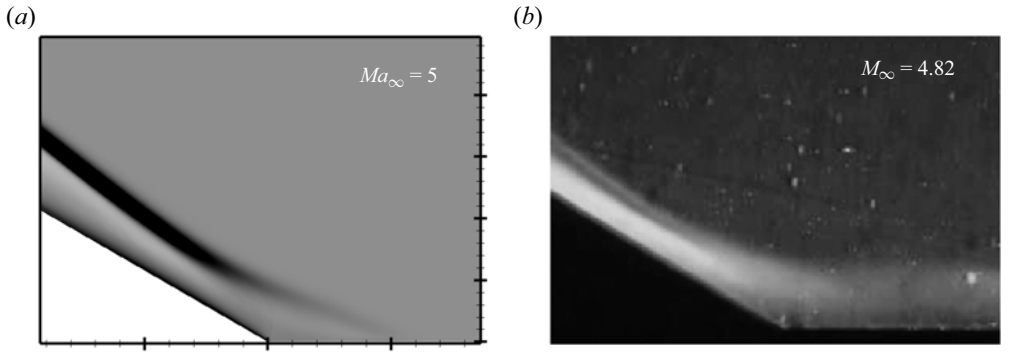

Figure 13. Present numerical schlieren visualization of shock wave structure (*a*) compared with the experiment result of Li (2007) (*b*).

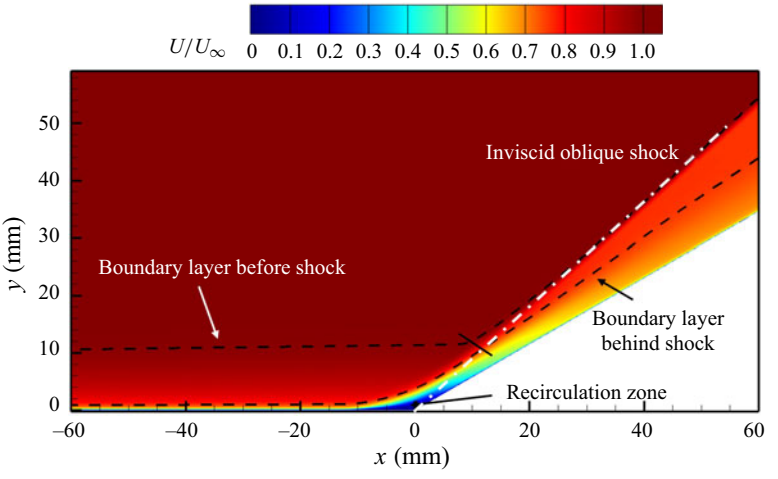

Figure 14. Basic structures in the flow field of the STBLI generated from the compression ramp.

and agrees well with the inviscid theory for the mainstream away from the wall with the near-wall boundary layer in a state of small separation.

The pressure ratio and interaction length are another two key parameters to describe the STBLI, which are shown in figure 15(*a*). Generally, the pressure ratio is used to describe the shock wave strength and the pressure ratio of the present DNS agrees well with the prediction of the inviscid oblique shock wave theory with the pressure ratio of 13. Note that in figure 15(*a*), and later similar figures of the streamwise distribution, when $x \leq 0$, this is equal to the global horizontal coordinate and, when $x > 0$, this represents the local coordinate x_r along the ramp wall as shown in the figure 15(*a*). Since there must be a subsonic region at the bottom of the boundary layer due to the no-slip wall condition, the high pressure propagates upstream and, hence, another important parameter in the STBLI is the upstream interaction length that is defined as the distance from the point where the pressure starts to rise to the starting point of the ideal shock wave (which here is the corner vertex). Souverein, Bakker & Dupont (2013) made an intelligent theoretical analysis of the interaction length in the STBLI and proposed a simple prediction method that established the relation between the dimensionless interaction length L^* and the dimensionless shock intensity S_e^*. Later, Jaunet, Debieve & Dupont (2014), Hong, Li & Yang (2021),

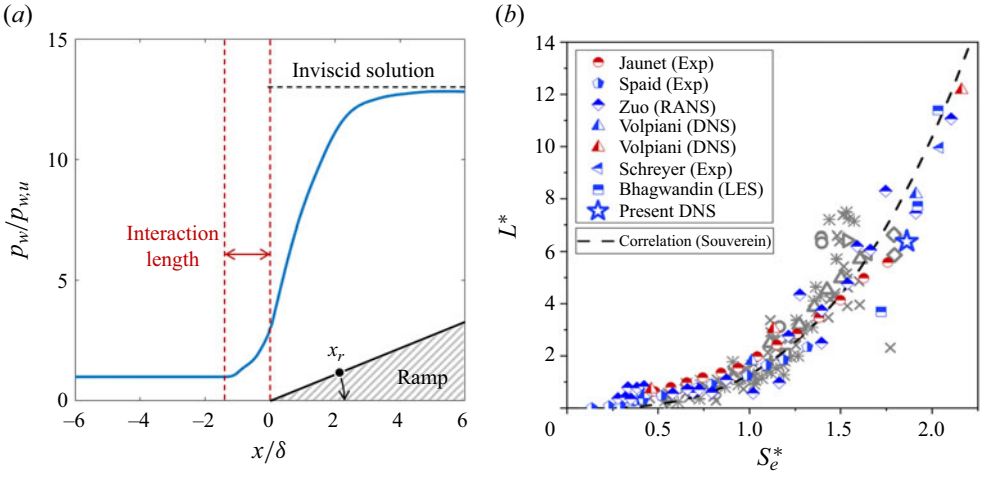

Figure 15. (*a*) Mean wall pressure through interaction and (*b*) interaction length compared with the previous prediction (Souverein *et al.* 2013) and data (the grey symbols are from Souverein *et al.* 2013, for adiabatic cases, the red symbols represent hot wall conditions and the blue symbols represent cold wall conditions).

Zuo *et al.* (2022), Volpiani *et al.* (2020) have corrected the relation for non-adiabatic wall conditions and hypersonic conditions. This paper uses the non-adiabatic wall corrected S_e^* proposed by Jaunet *et al.* (2014) and the result is shown in figure 15(*b*) with the previous results compiled by Souverein *et al.* (2013) and the recent non-adiabatic cases of Jaunet *et al.* (2014), Spaid & Frishett (1972), Schreyer *et al.* (2018), Bhagwandin, Helm & Martin (2019), Volpiani *et al.* (2020) and Zuo *et al.* (2022). The Souverein's correlation, $L^* = 1.3S_e^{*3}$, is also plotted in the same figure as a dotted line. The present DNS result is in the trend shown by all the previous data, especially by non-adiabatic ones, which indicates the present result is qualitatively reasonable. Compared with the Souverein's theory, the predicted interaction length is 18 mm while the present DNS results is 14 mm, with a relative deviation of 20 %. Considering that Souverein's fitting formula still contains some uncertainty and the fitting data have some scattering, this deviation can be considered reasonable. Besides, no plateau area is observed in the pressure distribution, indicating that the separation is in the incipient separation state. Above all, the calculated pressure ratio and interaction length in the STBLI are also generally consistent with previous theories.

In conclusion, the above analysis proves that the DNS results are physically reasonable and reliable again, and indicates that the STBLI in this work is in the initial separation state.

3. Theory of aerodynamic heating analysis

In this section we aim to develop a theoretical method to predict the peak heat flux ratio in the STBLI and to further provide an analytical method to explain the underlying reasons behind the peak heat flux in the STBLI. The prediction method is derived from the supersonic turbulent boundary layer theory and the oblique shock wave theory. Furthermore, the analytical method is obtained from the aerodynamic heat transport equation in turbulent flows with its underlying influence mechanisms on the wall heat flux. The theories discussed here are the basis of the DNS result analysis in the next section.

3.1. *Wall heat flux prediction*

The wall heat flux in the turbulent boundary layer can be predicted accurately with the current theory (van Driest 1956; Qu *et al.* 2001), so the essential question of the wall heat flux prediction in the STBLI lies in how many times the heat flux increases across the shock.

As reviewed in the introduction, Q-P theory is a method to predict the wall heat flux ratio in STBLIs in which the basic idea is to associate the heat flux ratio Q with the pressure ratio P in the interaction area. However, some recent studies have shown that the canonical QP85 theory has some deviations in some cases (Priebe & Martín 2021; Helm & Martín 2022; Tong *et al.* 2022*b*). To evaluate the QP85 theory more comprehensively, the data of Q and P have been collected from as much public literature as the authors are aware of, which supplements the highly cited but old datasets of Holden (1972). As shown in figure 16, the open symbols represent data from the collection of Holden (1972) that originally came from Levin & Fabish (1962), Sayano, Bausch & Donnelly (1962), Magnan & Spurlin (1966), while the solid symbols represent data from recent studies (Coleman & Stollery 1972; Holden 1972, 1977; Hayashi, Sakurai & Aso 1986; Delery & Coet 1991; Schülein 2006; Bernardini *et al.* 2016; Volpiani, Bernardini & Larsson 2018; Volpiani *et al.* 2020; Priebe & Martín 2021; Helm & Martín 2022; Tong *et al.* 2022*b*). The symbol colour reflects the Mach number (except for the red one that represents the present DNS result). It is easy to find that the classical QP85 prediction is obviously higher than the heat flux ratio in recent studies, especially for hypersonic flows. Quantitatively, the maximum relative error exceeds 70 %. According to recent studies, the deviation can be attributed to the different mainstream Mach number and the wall temperature. Therefore, in this work we have conducted a theoretical analysis based on the boundary layer thickness change to develop a more elaborate prediction method of the wall heat flux ratio in STBLIs.

Assuming that the heat transfer theory in compressible turbulent boundary layers still remains valid after boundary layers pass through shock waves, then the Stanton number at the reference temperature (Eckert 1960) should be proportional to the dimensionless boundary thickness, which leads to

$$\frac{St_d^*}{St_u^*} = \frac{\delta_d/x_d}{\delta_u/x_u}, \tag{3.1}$$

where $St \equiv q_w/[\rho_e U_e(H_r - H_w)]$, δ is the boundary layer thickness and x is the effective developing length of the boundary layers. The subscript u represents the parameters in the undisturbed boundary layer before shock waves while the subscript d represents the parameters in the disturbed boundary layer after shock waves, as also illustrated in figure 17. The subscript e represents the parameters at the edge of boundary layers while the subscript w represents the parameters on the wall. The superscript $*$ represents the parameters at the reference temperature that can be calculated as (Eckert 1960)

$$\frac{T^*}{T_e} = \frac{1}{2}\left(\frac{T_w}{T_0} + 1\right) + \frac{\gamma - 1}{4} Ma_e^2 \left(0.44r + \frac{T_w}{T_0}\right), \tag{3.2}$$

where r is the recovery coefficient and $r = Pr^{1/3}$, T_0 is the total temperature, γ is the specific heat ratio and set to 1.4. The left-hand side of (3.1) includes the heat flux ratio that is the target quantity and the right-hand side needs to be further handled.

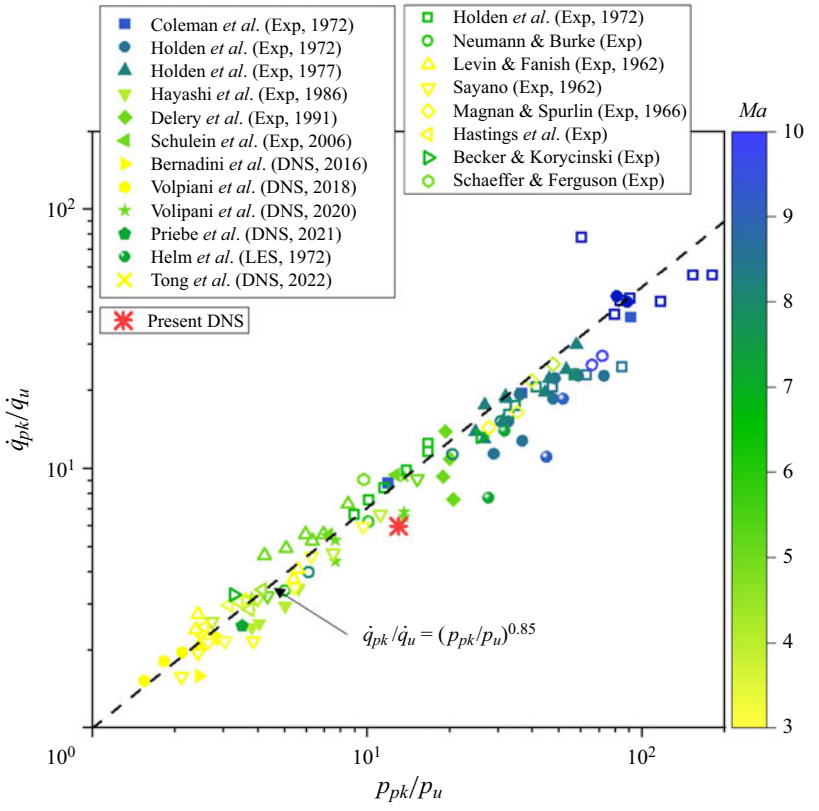

Figure 16. The relationship between peak heat flux ratio and peak pressure ratio in turbulent STBLI for a wide range of Ma.

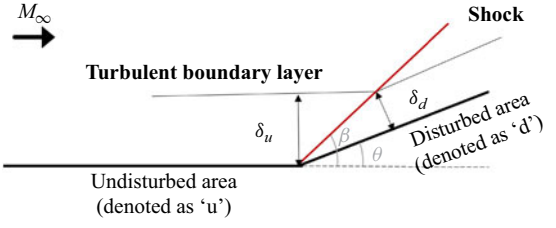

Figure 17. Definition of parameters in the STBLI for the theoretical analysis.

Assuming that the separation is not significant so that the flow structures can be described by figure 17, then the following geometric relation can be obtained:

$$\frac{\delta_d}{\delta_u} = \frac{\sin(\beta - \theta)}{\sin(\beta)}. \tag{3.3}$$

Here β is the shock angle and θ is the turning angle. According to the oblique shock relation, the angles can be substituted by the pressure ratio p_d/p_u and the incoming Mach

number Ma_u:

$$\frac{\sin(\beta-\theta)}{\sin(\beta)} = \frac{Ma_u\left[(\gamma+1)-(\gamma-1)\dfrac{p_d}{p_u}\right]}{\left[Ma_u^2\left((\gamma+1)\dfrac{p_d}{p_u}+(\gamma-1)\right)-2\left(\left(\dfrac{p_d}{p_u}\right)^2-1\right)\right]^{1/2}\left[(\gamma+1)\dfrac{p_d}{p_u}-(\gamma-1)\right]^{1/2}}. \tag{3.4}$$

The effective developing length can be solved by the reference temperature method

$$\frac{\delta_d/x_d}{\delta_u/x_u} = \left(\frac{Re^*_{x_d}}{Re^*_{x_u}}\right)^{-0.2}, \tag{3.5}$$

from which then

$$\frac{x_d}{x_u} = \left(\frac{\delta_d}{\delta_u}\right)^{1.25}\left(\frac{\rho_{ed}U_{ed}}{\rho_{eu}U_{eu}}\right)^{0.25}\left(\frac{\mu_d}{\mu_u}\right)^{-0.25}\left(\frac{(T^*/T_e)_d}{(T^*/T_e)_u}\right)^{-0.25(1+\omega)}, \tag{3.6}$$

where ω is the viscosity–temperature exponent based on the assumption that viscosity satisfies the power relation with temperature and ω is set to 0.78 here. Finally, incorporating (3.3) and (3.6) into (3.1) and ignoring the change of the recovery temperatures and the mainstream velocities, then

$$\frac{\dot{q}_d}{\dot{q}_u} = \left(\frac{\sin(\beta-\theta)}{\sin(\beta)}\right)^{-0.25}\left(\frac{\left(1+\dfrac{T_w}{T_0}\right)+0.2Ma_d^2\left(0.44r+\dfrac{T_w}{T_0}\right)}{\left(1+\dfrac{T_w}{T_0}\right)+0.2Ma_u^2\left(0.44r+\dfrac{T_w}{T_0}\right)}\bullet\frac{1+0.2Ma_d^2}{1+0.2Ma_u^2}\right)^{0.25\omega-0.75} \times\left(\frac{p_d}{p_u}\right)^{0.75}. \tag{3.7}$$

Furthermore, the Mach number after shock waves, Ma_d, in (3.7) can also be substituted by the pressure ratio p_d/p_u and the incoming Mach number Ma_u according to the oblique shock relation:

$$Ma_d^2 = \frac{Ma_u^2\left[(\gamma+1)\dfrac{p_d}{p_u}+(\gamma-1)\right]-2\left[\left(\dfrac{p_d}{p_u}\right)^2-1\right]}{\dfrac{p_d}{p_u}\left[(\gamma+1)+(\gamma-1)\dfrac{p_d}{p_u}\right]}. \tag{3.8}$$

In summary, (3.7) combined with (3.4) and (3.8) relates the wall heat flux ratio $\dot{q}_d/\dot{q}_u$ to the pressure ratio p_d/p_u, incoming Mach number Ma_u and the wall temperature T_w/T_0. According to this formula, the peak heat flux ratio can be predicted for different peak pressure ratios at different Ma_u and T_w/T_0 as shown in figure 18. The results indicate that the heat flux ratio is strongly related to the pressure ratio, although the relation between them in (3.7) is not a simple power relation. The results show that the heat flux ratio is

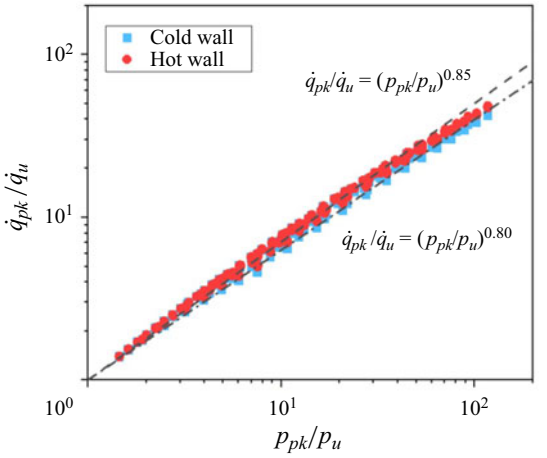

Figure 18. Present heat flux ratio prediction according to the present correlation, (3.7), for sample points at Ma_u of 3–15 and T_w/T_0 of 0.2–0.8 (for cold wall in blue) or 1.2–1.8 (for hot wall in red).

approximately 0.85 power of the pressure ratio for the hot wall conditions and 0.8 power for the cold wall conditions.

The accuracy of (3.7) is further evaluated by comparing with the data in previous literature, in which the data source is the same as in figure 16. The results show that the present heat flux ratio prediction reduces the relative error from 72 % to 35 %, compared with the canonical QP85 correlation as shown in figure 19. More detailed comparisons are provided in figure 20 where the wall heat flux distribution along the streamwise direction is predicted by the wall pressure distribution for the representative experiments of Delery & Coet (1991), Coleman & Stollery (1972) and Schülein (2006), respectively. In figure 20(*a*) there is no distinct separation area in the STBLI, the increase and the peak of the wall heat flux are well predicted compared with experimental results. In figure 20(*b*) there is a small separation bubble and the wall heat flux is also well reproduced by the present correlation. In figure 20(*c*) the prediction of the STBLI induced by a 10° shock generator is consistent with the experimental result while the prediction of the STBLI induced by a 14° shock generator also gives a reasonable heat flux peak but shows some deviation in the separation area. In conclusion, the present correlation can predict the wall heat flux ratio and its distribution in the STBLI with relatively high accuracy.

Reviewing the physical meaning of (3.7) from the derivation process, the term in the first bracket on the right represents the heat transfer enhancement caused by boundary layer compression due to *Ma* decrease. The term in the second bracket reflects the wall temperature effect on the STBLI by influencing the compressible boundary layer before and behind the shock. The complex coupling effect of the wall temperature on the interaction area is not considered in the present theoretical derivation, which makes the prediction not sensitive enough to the wall temperature for some cases and requires improvements in future research. The term in the third bracket represents the heat transfer enhancement caused by the enhancement of the fluid heat transport capacity due to the density increase. Therefore, from this perspective, the sharp increase of the heat flux in the STBLI is caused by the compression of boundary layers and the density increase in the mainstream.

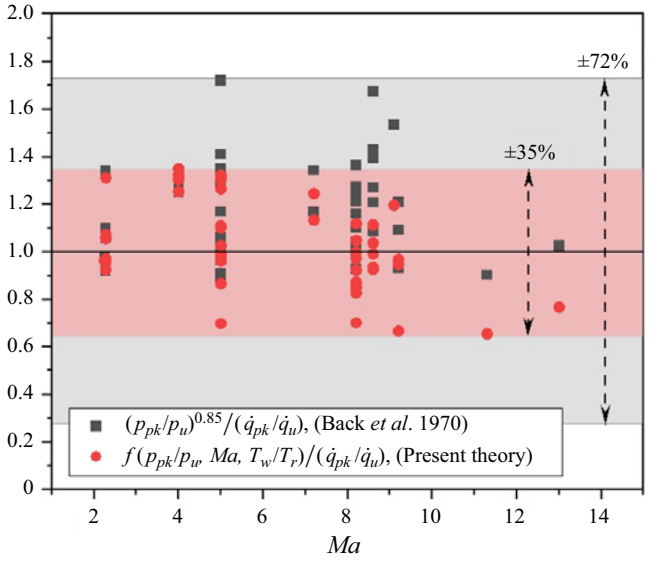

Figure 19. Present heat flux ratio prediction accuracy of the previous studies compared with the canonical QP85 correlation. (The data are from the same source as figure 16.)

3.2. *Turbulent aerodynamic heat transport equation*

The generation and transport process of aerodynamic heat are further investigated, which are controlled by the aerodynamic heat transport equation. The average heat transport governing equation is introduced in this subsection, while the corresponding DNS statistic results are given and discussed in the next section.

The derivation begins with the enthalpy transport equation that can be derived from the momentum conservation and energy conservation equations, which is

$$\frac{\partial \rho h}{\partial t} + \frac{\partial \rho u_j h}{\partial x_j} = \frac{\partial p}{\partial t} + u_j \frac{\partial p}{\partial x_j} + \tau_{ij} S_{ij} + \frac{\partial}{\partial x_j}\left(\lambda \frac{\partial T}{\partial x_j}\right), \tag{3.9}$$

where according to Newtonian fluid constitutive relation,

$$\tau_{ij} = 2\mu S_{ij}^d, \tag{3.10}$$

where S_{ij}^d is the deviatoric part of the shear rate tensor S_{ij}, that is, $S_{ij}^d \equiv S_{ij} - (S_{kk}/3)\delta_{ij}$.

Reynolds averaging is carried out for (3.9) and the Favre averaging, i.e. density-weighted averaging, is used on the left to avoid producing too many terms. Following the common custom, $\bar{q}$ represents the Reynolds average value of q while q' represents corresponding fluctuation; $\tilde{q}$ represents the Favre average value of q while q'' represents corresponding fluctuation. Since this work is *a posteriori* analysis based on DNS statistics, the existence of both Reynolds and Favre averages does not cause any problems regarding reaching a closed-form solution. Assuming the flow field to be statistically steady and the correlation between fluctuations of physical properties and flow variables can be ignored, then

$$\frac{\partial \bar{\rho} \widetilde{u_j} \tilde{h}}{\partial x_j} + \frac{\partial \bar{\rho} \widetilde{u_j'' h''}}{\partial x_j} + \frac{\partial}{\partial x_j}\left(-\bar{\lambda} \frac{\partial \bar{T}}{\partial x_j}\right) = \overline{u_j} \frac{\overline{\partial p}}{\partial x_j} + \overline{u_j' \frac{\partial p'}{\partial x_j}} + 2\bar{\mu} \overline{S_{ij}^d S_{ij}^d} + 2\bar{\mu} \overline{S_{ij}^{d'} S_{ij}^{d'}}. \tag{3.11}$$

Non-dimensionalize the above equation with corresponding incoming values (i.e. ρ_∞, U_∞, T_∞, $\rho_\infty U_\infty^2$, μ_∞) and unit length $L_{ref} = 1$ mm, remain the original symbols for

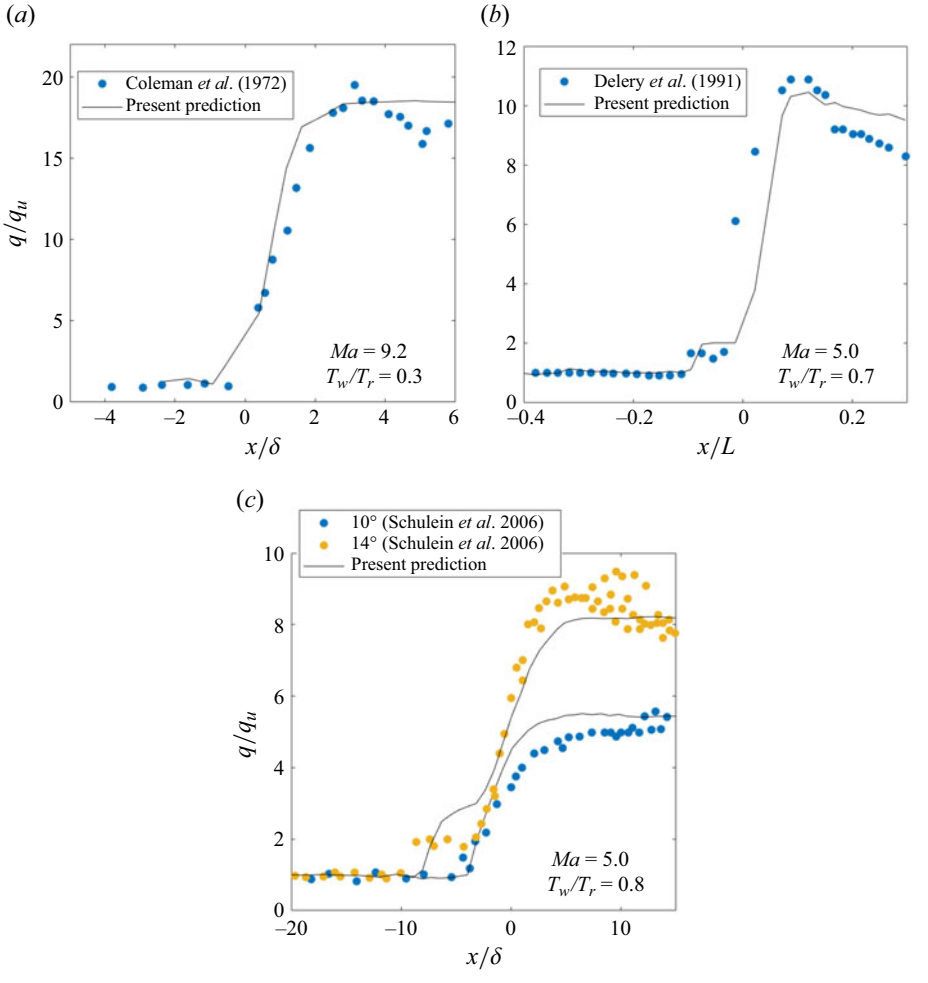

Figure 20. Present heat flux distribution prediction, (3.7), for three representative experiments (Coleman & Stollery 1972; Delery & Coet 1991; Schülein 2006).

simplicity, and the dimensionless form of (3.11) can yield

$$\underbrace{\frac{\partial \bar{\rho}\widetilde{u}_j\widetilde{T}}{\partial x_j}}_{\nabla\cdot q_c}+\underbrace{\frac{\partial \bar{\rho}\widetilde{u_j''T''}}{\partial x_j}}_{\nabla\cdot q_t}+\underbrace{\frac{1}{PrRe}\frac{\partial}{\partial x_j}\left(-\bar{\mu}\frac{\partial \bar{T}}{\partial x_j}\right)}_{\nabla\cdot q_v}=\underbrace{(\gamma-1)Ma^2\left(\overline{u_j}\frac{\overline{\partial p}}{\partial x_j}+\overline{u_j'}\frac{\overline{\partial p'}}{\partial x_j}\right)}_{H_{p,m}+H_{p,t}}+\underbrace{\frac{(\gamma-1)Ma^2}{Re}(2\bar{\mu}\overline{S_{ij}^dS_{ij}^d}+2\bar{\mu}\overline{S_{ij}^{d'}S_{ij}^{d'}})}_{\Phi_m+\Phi_t}. \tag{3.12}$$

Equation (3.12) has a clear physical interpretation: the right-hand side is the generation terms of aerodynamic heat while the left-hand side is the transport terms of aerodynamic heat. Here $H_{p,m}$ is the directional derivative of the average pressure along the average streamlines and represents the aerodynamic heat generated by the average compression;

$H_{p,t}$ is aerodynamic heat generated by fluctuation compression. The generation of compression aerodynamic heat will be dominant near the stagnation region or where there are obstacles. Here Φ_m is aerodynamic heat caused by mean shear dissipation while Φ_t is aerodynamic heat caused by the turbulent shear dissipation. Even though the turbulent fluctuations are not significant in certain situations, the turbulent shear dissipation is still considerable due to the turbulence on a very small spatial scale. Additionally, although both types of aerodynamic heat are converted from kinetic energy, the generation of compression aerodynamic heat is reversible while the generation of dissipation aerodynamic heat is irreversible. For the left-hand side of the equation, the first is the mean convective transport, the second is the turbulent transport and the third is the molecular viscous transport. Here $\boldsymbol{q_c}$, $\boldsymbol{q_t}$ and $\boldsymbol{q_v}$ are the convective heat flux, turbulent heat flux and viscous heat flux, respectively. On the wall, the average convective and turbulent heat transport are both zero and, hence, the total heat flux is only contributed by viscous transport. However, the viscous flux on the wall is relatively passive and the analysis of the distribution of each heat transport term in the flow field is helpful to more comprehensively understand the heat transfer process.

In conclusion, (3.12) shows that the flow generates aerodynamic heat through compression and dissipation, which is then transported through mean convection, turbulent fluctuation and viscous conduction in the fluid. Although the heat is seemingly transferred only through viscous conduction on the wall, all generation and transport processes influence the viscous conduction and, hence, the wall heat flux.

4. Mechanisms of aerodynamic heating enhancement

In this section the wall heat flux distribution in the STBLI is comprehensively analysed. Furthermore, the generation and near-wall transport processes of aerodynamic heat are investigated from both average flow and turbulence perspective, which reveals the underlying mechanisms of the wall heat flux distribution, especially the wall heat flux peak in the STBLI.

4.1. *Wall heat transfer enhancement*

Across the interaction, the wall heat flux is six times stronger than the incoming value and the increase process is greatly different from the skin friction as shown in figure 21(*a*). There is a local minimum before the heat flux jump, which basically coincides with the average separation point position. The heat flux across the interaction jumps sharply and a wide peak appears downstream of the reattachment point. In the convective heat transfer investigation, the Reynolds analogy is a widely used method, which suggests that St shows similar behaviours as C_f or in other words the Reynolds analogy factor $S \equiv C_f/2St$ is constant. However, the DNS results show that the wall heat transfer increases while the skin friction decreases around the corner. As can be seen more clearly from figure 21(*b*), the Reynolds analogy factor deviates from the value of 0.86 in the turbulent boundary layer (Qu *et al.* 2001) and changes drastically across the interaction, especially in the recirculation region. Interestingly, although the Reynolds analogy factor reaches constant downstream, it does not recover to the undisturbed value and stays at 0.5. This phenomenon is also reported by Helm & Martín (2022), which is not well understood in current research and is open to be studied. As for the failure of the Reynolds analogy, it is not surprising due to the strong adverse pressure gradient and, thus, highlights the need to develop other wall heat flux prediction methods in the STBLI.

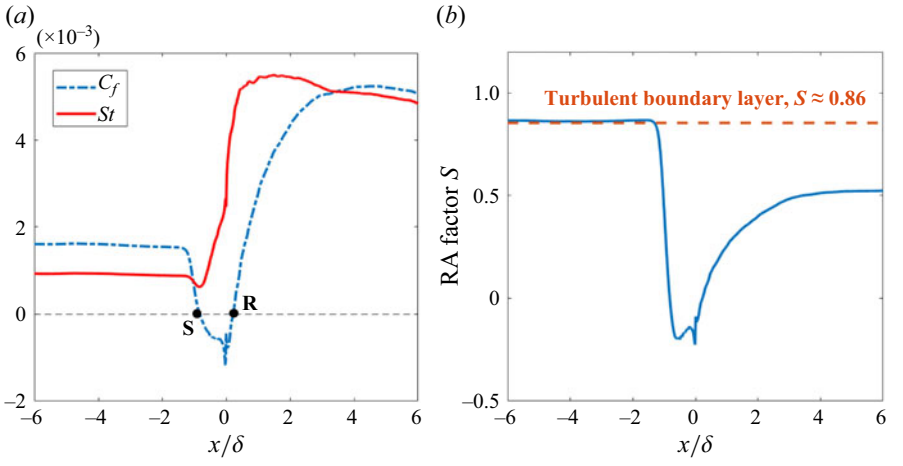

Figure 21. Stanton number and failure of Reynolds analogy through interaction.

As mentioned in the previous section, the heat flux change is strongly related to the pressure change and, hence, the DNS results are investigated from the present correlation (i.e. (3.7)). The wall heat flux is non-dimensionalized by q_u, the wall heat flux at the reference position of the undisturbed boundary layer, and is then converted to a ratio as shown in figure 22. At the same time, (3.7) is used to predict the heat flux ratio for the same conditions as the DNS in this work. The pressure p_d is replaced by the wall pressure p_w and the pressure p_u is replaced by the reference pressure at $x = -60$ mm. The prediction result of the present theory is provided in figure 22 with the theoretical prediction of Coleman & Stollery (1972). The results show that both theories are in good agreement with the DNS result before the reattachment point, but the prediction results are higher downstream. The relative deviation of the peak heat flux ratio between the present theory and the present DNS is 23 % while the prediction of Coleman & Stollery (1972) is 34 %. The relative deviation is acceptable according to the analysis in § 3 where the paper claims that the relative error of the present theory is under 35 %. The quantitative analysis suggests that the present theory is able to explain the heat flux jump in the STBLI in present DNS. Therefore, the theoretical and computational results show that the key reasons of wall heat flux jumps in the STBLI are the boundary layer compression and the mainstream density increase caused by shock waves.

4.2. *Aerodynamic heat generation and near-wall transport*

To further reveal the mechanisms of the wall heat flux changes in the STBLI, all generation and transport terms in the turbulent aerodynamic heat transport equation (3.12) are calculated statistically during the time advance of DNS, and then the generation and near-wall transport process of aerodynamic heat are quantitatively analysed in different regions in detail.

The detailed distribution of aerodynamic heat generation around the corner are shown in figure 23 where the y axis is stretched for better presentation of the near-wall characteristic. Dissipation aerodynamic heat is displayed in the first line while compression aerodynamic heat is displayed in the second line. For the dissipation aerodynamic heat as shown in figure 23(*a*), the generation rate increases and the generation area expands significantly, which leads to increased total heat generation. Interestingly, the peak location of the

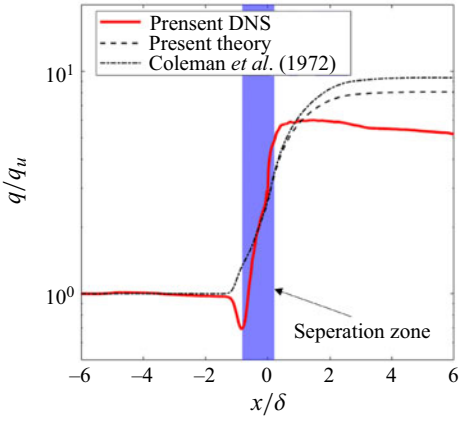

Figure 22. Heat transfer on the wall through interaction compared with previous theoretical predictions and present theoretical predictions.

dissipation aerodynamic heat shows clear dependency on the detachment and reattachment of the shear layer. The dissipation aerodynamic heat is further decomposed by Reynolds averaging as shown in figure 23(*b*,*c*). It can be found that the dissipation heat in the undisturbed boundary layer is mainly generated from the strong mean shear near the wall, while the dissipation heat generation is dominated by turbulence in the interaction area. As the shear layer detaches and reattaches, two heating cores appear in the near-wall region, indicating that the turbulent dissipation enhancement in the recirculation region is related to the enhancement of the shear turbulence, which can further be attributed to the Kelvin–Helmholtz instability. For the compression aerodynamic heat, as shown in figure 23(*d*), the generation rate is extremely high in the interaction area due to the shock compression, which is the clear feature of the STBLI distinguished from the boundary layer. Note that the compression aerodynamic heat is relative to the local flow velocity, hence, the compression heat area is lifted up and away from the wall slightly due to the low-speed recirculation bubble in the corner. At downstream of the corner, strong compression heat is continuously generated near the wall because the flow is reattached and the hypersonic shock layer is close to the wall. Likewise, the compression aerodynamic heat is further decomposed by Reynolds averaging as shown in figure 23(*e*,*f*). It can be found that the compression heat is mainly generated from the deceleration and compression of the mean flow. The fluctuating compression heat between positive and negative values is generated around the theoretical shock, indicating that the shock wave is unstable, which also poses an interesting question but is outside the scope of this paper. In summary, in the STBLI area the generation of aerodynamic heat increases significantly, which is mainly due to the heat generated by the increased turbulent dissipation and the average flow deceleration and compression.

The heat transport results in the near-wall region are presented by heat flux lines with intensity distribution as shown in figure 24 where the y-axis scale is not stretched and remains equal to the x axis to ensure the orthogonality of the coordinate system. Note that the density of the heat flux lines in the figure cannot represent heat flux intensity because each heat flux is not conserved due to the generation of aerodynamic heat and the transformation of different transport modes. The hot area is the near-wall area and separation area as shown in the temperature field. In the figure the gradient field is also shown and a distinct feature of the distribution is that an adiabatic line divides the

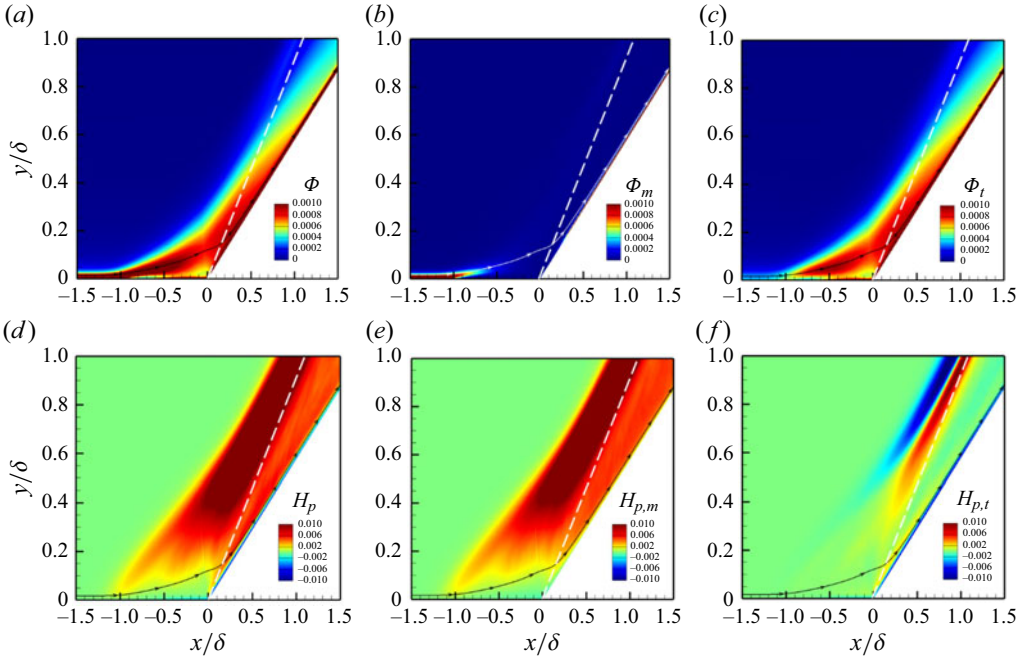

Figure 23. Aerodynamic heat with its Reynolds-average decomposition. Plots (*a–c*) are dissipation aerodynamic heat while plots (*e–f*) are compression aerodynamic heat. (White dash lines represent theoretical shock while the near-wall streamlines represent shear layer.)

temperature field into two regions, which corresponds to the single-peak distribution feature of the near-wall temperature profile. The distribution of the conduction and turbulent heat flux line also has an adiabatic line and shows a similar feature. For the conduction transport, the heat is transported to the mainstream above the adiabatic line while the heat is transported to the wall under the line. The magnitude of the conduction heat flux has a peak band above and below the adiabatic line, showing a bimodal feature. For the turbulence transport, heat is transported upstream in most areas while heat is transported to the wall in the extreme near-wall region. The reason for this is that the turbulent heat flux lines are affected by both the mean flow field and the temperature gradient field, and the turbulence intensifies the heat exchange in the streamwise direction. The magnitude of the turbulent heat flux is strong in the compression area and the extreme near-wall area on the ramp. For the convection transport, the mean convection heat flux lines are close to the mean flow lines, which also indicates the Favre-averaged velocity field is similar to the Reynolds averaged velocity field in the present study. The aerodynamic heat is transported downstream with mean convection in the mainstream. In the recirculation near the wall, the aerodynamic heat is transported downstream at the outer edge and transported upstream at the bottom, which strengthens the mixing of the aerodynamic heat near the wall. In summary, focusing on the near-wall region within the adiabatic lines in the STBLI, the conduction dominates the heat transport to the wall in the extreme near-wall region, the turbulence in the near-wall region transfers heat to the extreme near-wall region and the mean convection strengthens the mixing of upstream and downstream aerodynamic heat.

To further investigate the aerodynamic heat generation and transport process, the heat budgets with the velocity and temperature profiles at five key positions are shown in

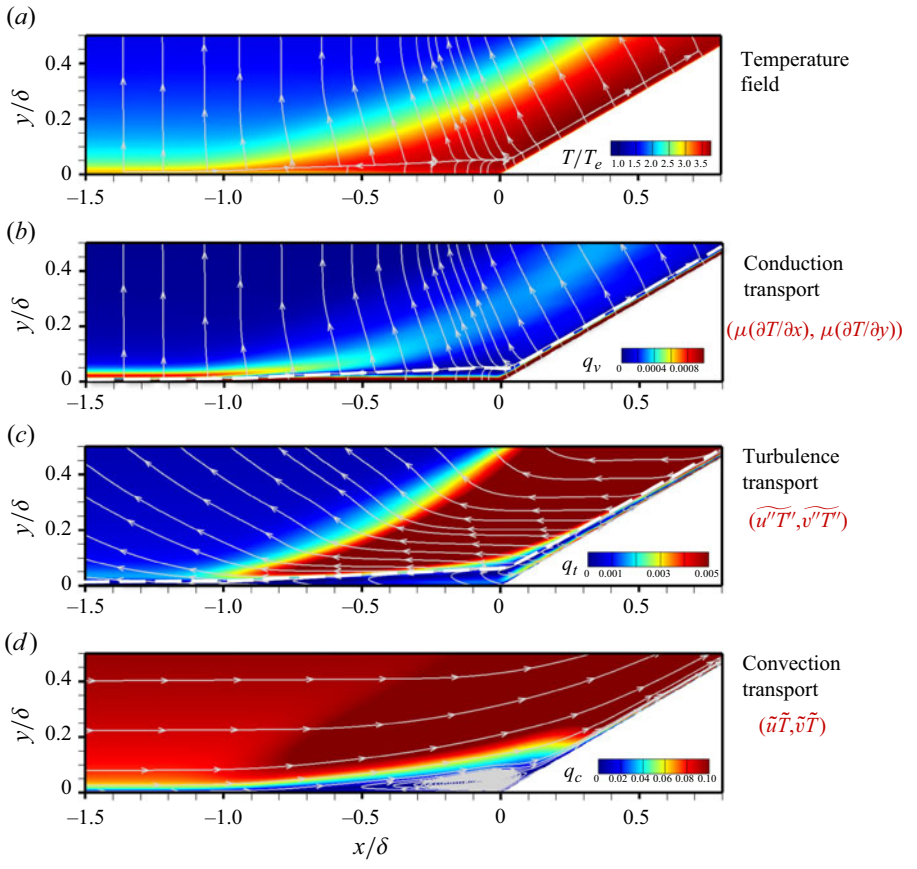

Figure 24. Temperature distribution and three transport mechanisms presented by heat flux lines with their magnitude distribution through interaction in near-wall region.

figures 25 and 26 where the horizontal coordinate, y, is the normal distance away from the wall and dimensionless with the viscous scale δ_v at the reference position. Two key positions are selected in the turbulent boundary layer and the other three are in the STBLI area, which will be discussed respectively below. The black lines in the figure represent the sum of all the terms and the results indicate that the sum is around zero for every key position, which means the statistic results have reached balance.

In the turbulent boundary layer the aerodynamic heat is mainly generated by dissipation and transported by turbulence and viscous conduction as shown in figure 25. Figure 25(*a*,*b*) shows the aerodynamic heat budgets in the boundary layer upstream ($x/\delta = -6$) and downstream ($x/\delta = 6$) of the shock wave. Note that the y-coordinate scale in figure 25(*b*) is one order of magnitude larger than figure 25(*a*). Due to the high shear in the hypersonic flow near the wall, the aerodynamic heat is mainly generated by mean dissipation in the viscous sublayer. Since there is no significant pressure change in the flat plate boundary layer, the aerodynamic compression heat is around zero. In the viscous sublayer, viscous conduction dominates the heat transport and the output energy from the viscous conduction is transferred to the wall. In the buffer layer the generated aerodynamic heat is transported mainly by turbulent fluctuation toward the wall and the main flow, which is because the buffer layer is a region of active turbulence and peak temperature

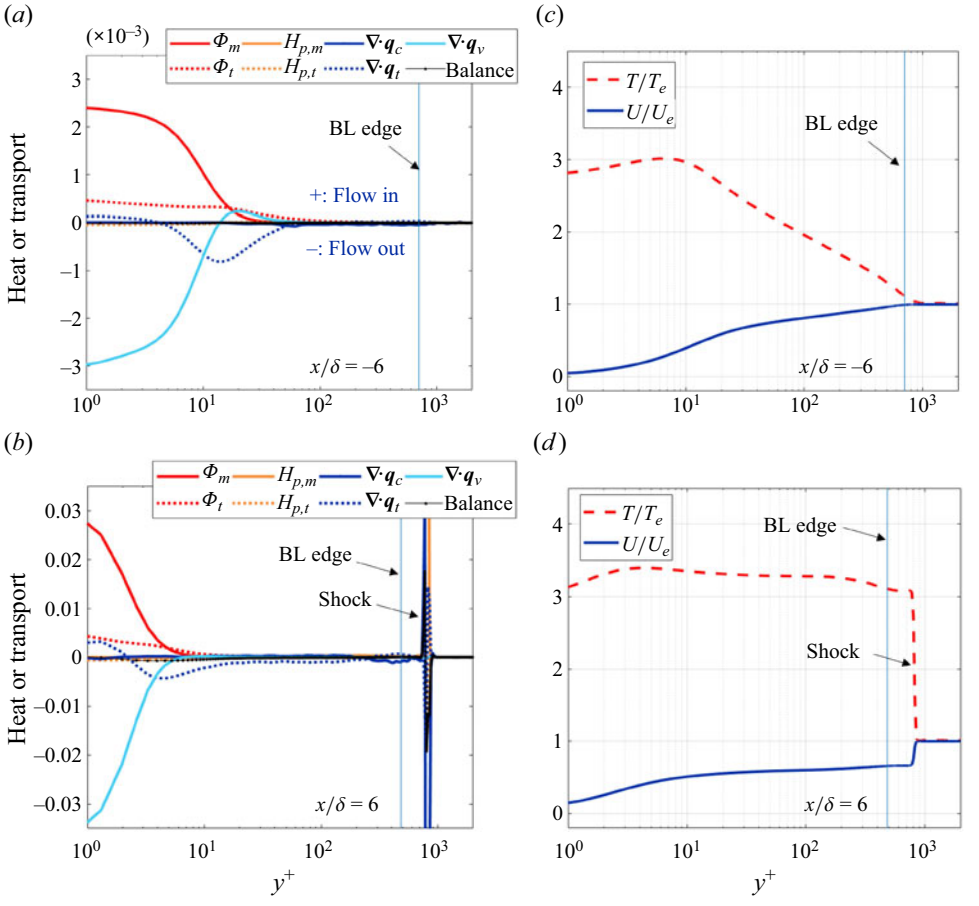

Figure 25. Aerodynamic heat generation and transport budget in the turbulent boundary layer at (*a*) $x/\delta = -6$ and (*b*) $x/\delta = 6$ with (*c*,*d*) the corresponding temperature and velocity profiles. Symbols in the legends of (*a*,*b*) are defined in (3.12).

as shown in figure 25(*c*). In the logarithmic layer the aerodynamic heat generation and transport are both less active. Before and behind the shock wave, the aerodynamic heat generation and transport in the boundary layer are qualitatively similar, but quantitatively quite different. Post reattachment, the heat generated by dissipation is closer to the wall and the intensity increases by nearly one order of magnitude while the turbulent transport and the viscous transport near the wall are also greatly strengthened. All of this can be attributed to the compression of boundary layers that make the shear increase dramatically after shock waves.

In contrast to the turbulent boundary layer, there exist significant compression aerodynamic heat generation and complex mean convective transport in the STBLI area that make the heat budget more complicated as shown in figure 26(*a–c*). The average compression aerodynamic heat at the three representative positions all show a peak value at the outer part of the boundary layer that indicates the position of the strong compression waves. The turbulent compression aerodynamic heat is not the dominant term near the wall and, hence, it will not be considered in this work. The clear differences in aerodynamic heat generation and transport between the separation region, recirculation region and

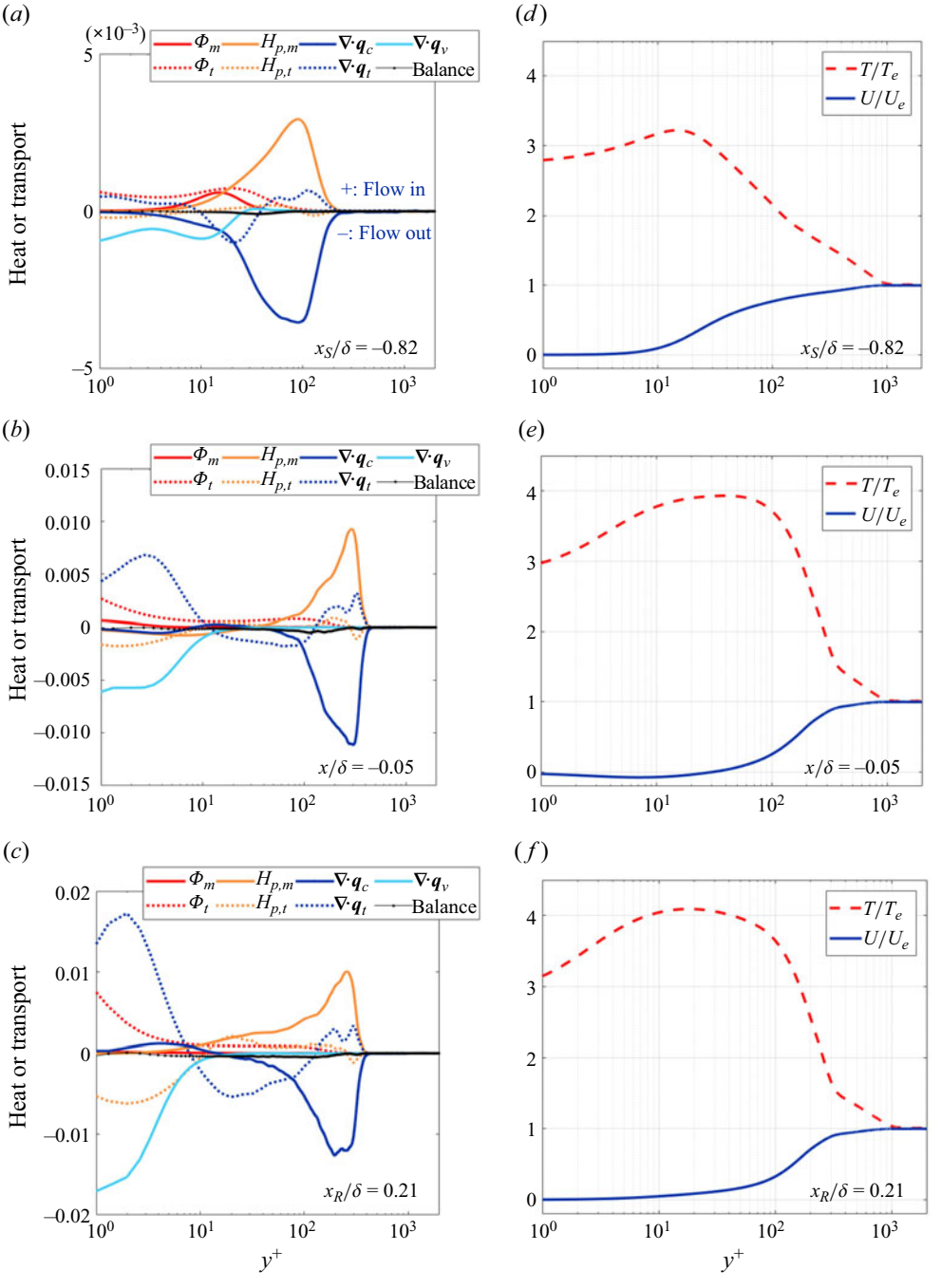

Figure 26. Aerodynamic heat generation and transport budget in the STBLI area at (*a*) separation point ($x/\delta = -0.82$), (*b*) recirculation centre ($x/\delta = -0.05$) and (*c*) reattachment point ($x/\delta = 0.21$) with (*d–f*) the corresponding temperature and velocity profiles. Symbols in the legends of (*a–c*) are defined in (3.12).

reattachment region reveal the underlying different wall heat flux mechanisms in these three regions.

At the separation point ($x_S = -0.82\delta$), the aerodynamic heat transport outward to the external flow is enhanced, which results in a local minimum of the wall heat flux. As shown in figure 26(a), compared with the undisturbed turbulent boundary layer, the average heat dissipation position at the separation point moves upward, which is associated with the upward shift of the shear layer. Meanwhile, the turbulent aerodynamic dissipation heat increases significantly with a peak value near $y^+ = 25$ and is larger than the average heat dissipation at all heights. The turbulent transport is active at all heights and becomes positive at the position of the compression wave, which means the heat is transported here by turbulence. Due to the shear layer uplift, more dissipation aerodynamic heat is transported to the outer boundary layer by the turbulent fluctuation and then balanced by the convective transport downstream together with the compression aerodynamic heat. Therefore, the aerodynamic heat transported to the wall decreases, which explains the local minimum of the heat flux at the separation point.

At the recirculation core ($x = -0.05\delta$) near the corner vertex, the active turbulence transports aerodynamic heat to the wall, which is generated by compression and turbulent dissipation, leading to the sharp increase of the wall heat flux. As shown in figure 26(b), the dissipation aerodynamic heat near the wall is mainly contributed by turbulent dissipation, which is related to the recirculation instability of the separation bubble in the STBLI and the near-wall backflow can also be seen clearly in figure 26(e). At the same time as the turbulent dissipation enhancement, the turbulent transport near the wall is also significantly enhanced. The range of near-wall transport is expanded due to the separation effect, which can also be explained by the higher and wider temperature peak as shown in figure 26(e). In the extreme near-wall region, the heat input from turbulent transport with the turbulent dissipation heat is balanced with the output through viscous transport. The heat input from turbulent transport comes from the turbulent dissipation of the shedding shear layer and the compression aerodynamic heat of the outer layer. The above analysis suggests such a mechanism for the heat flux jump around the corner: to increase the pressure, the relatively low-speed near-wall shear layer lifts up so that the momentum exchange is enhanced between the near-wall fluid and the main flow, which also enhances the heat exchange leading to the high temperature recirculation bubble and the sharp rise of the wall heat flux. The heat is generated from the turbulent dissipation as well as the compression of the shear layer and the exchange way is mainly the turbulent transport.

Near the reattachment point ($x_R = 0.21\delta$), the enhancement of near-wall dissipation and turbulent transport as well as the compression aerodynamic heat caused by oblique impingement in the attachment process lead to the wall heat flux rise and the peak a little downstream of the attachment point. In the reattachment region there exists aerodynamic heat generated by the compression of the local oblique impingement flow together with the compression aerodynamic heat transported from upstream through the mean convection, which is further transported to the near wall through the active turbulent fluctuation. When transferred to the vicinity of the viscous sublayer, the input heat is balanced with the output by viscous conduction. At the downstream of the reattachment point, the average shear starts to increase and the average dissipation heat increases accordingly. Simultaneously, the near-wall fluid is compressed in a wide range resulting in continuous compression aerodynamic heat generation, due to the wall restriction. Subsequently, the wall heat flux reaches a relatively wide peak. Finally, with the thickening and relaxation of the boundary layer, the wall heat flux begins to decline slowly. The generation and transport processes of compression aerodynamic heat described here also reveal the underlying mechanism

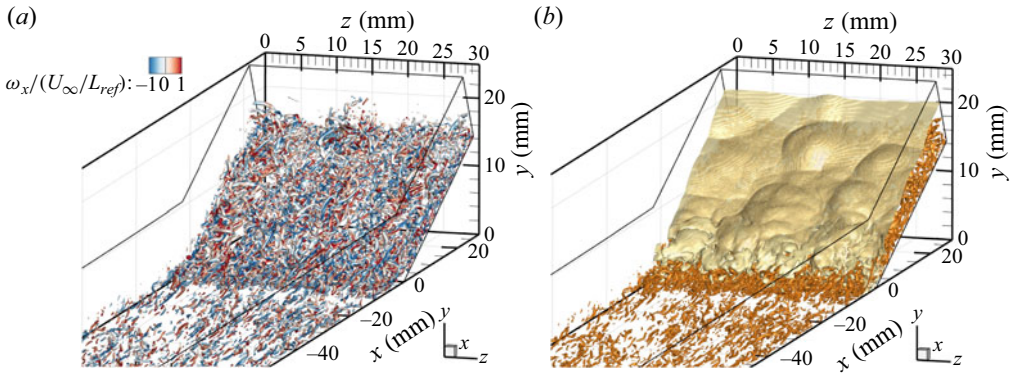

Figure 27. (*a*) Near-wall turbulent vortices coloured by the vorticity in the x direction and (*b*) instantaneous shock interacted with the vortices in the STBLI.

of the strong dependence of peak heat flux ratios to peak pressure ratios and these results provide theoretical support for the canonical Q-P correlation.

The above analysis indicates that the turbulence dominates the aerodynamic heating in the STBLI area and, hence, the turbulent vortices are further investigated, which provide a more fundamental perspective on the turbulent dissipation and turbulent transport. Turbulent vortices are extracted by the Q criterion as shown in figure 27 where the instantaneous shock wave is also presented, which is represented by the isosurface of pressure. The instantaneous shock wave is not an ideal flat thin layer. Pits appears in the bottom of the shock wave when the near-wall streamwise vortices pass through and the whole structure appears as small spanwise ripples. The main shock surface has bulging structures on the boundary layer scale, which are caused by the motion of coherent turbulent structures in the outer boundary layer. As for the near-wall vortices, the small-scale streamwise vortex pairs dominate the near-wall turbulence in the upstream undisturbed boundary layer. When passing through the shock wave, the vortices are enhanced, which suggests that the turbulent intensity is significantly enhanced. The streamwise vortices lift up and there appear many spanwise vortices, which are the characteristics of free shear layers (Brown & Roshco 1974; Roshco 1976). The changes of the vortices shed light on the enhancement of turbulent dissipation and transport in the recirculation and reattachment regions.

Finally, the mechanisms of aerodynamic heat generation and near-wall transport in different regions of the STBLI are summarized in figure 28. In the undisturbed boundary layer the aerodynamic heat is mainly generated by shear dissipation, which is transported to the wall by turbulent and viscous transport. However, the near-wall shear dissipation and turbulent transport are strengthened downstream of the shock wave, which causes the wall heat flux to reach a higher equilibrium level. Near the separation point, the enhanced heat transport to outer layers leads to the local minimum of the wall heat flux. In the recirculation region the high temperature separation bubble and the sharp rise of wall heat flux can be explained by the increasing aerodynamic heat generated by both dissipation and compression, and the enhancement of the heat exchange between the near-wall fluid and the outer fluid due to enhanced turbulence. The peak heat flux downstream of the reattachment point is due to the enhanced dissipation near the wall caused by shear layer reattachment, the compression heat brought from upstream and the local oblique impingement convection in the attachment process, and the near-wall turbulent transport enhancement as shown in the reattachment zone of the figure. The generation and

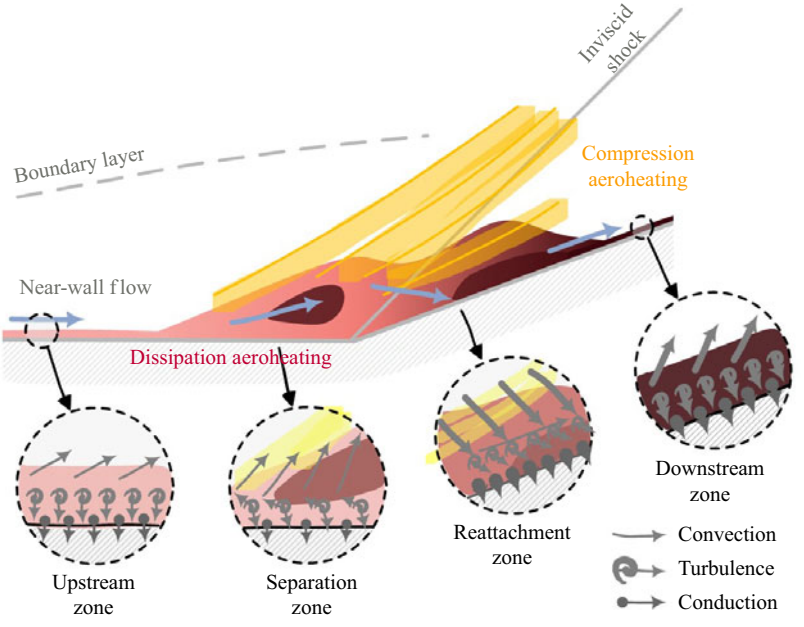

Figure 28. Sketch of the aerodynamic heat generation and transport process in the hypersonic STBLI (Aerodynamic heat is generated from dissipation in red and compression in yellow; aerodynamic heat is transported from convection, turbulence and conduction as shown by the legend and the arrow thickness represents the transport intensity.)

transport of compression aerodynamic heat reveal the underlying mechanism of the strong dependence of peak heat flux ratios to peak pressure ratios. In addition, the enhancement of turbulent dissipation and transport in the recirculation and reattachment regions can be explained by the intensified near-wall turbulent vortices during the interaction.

5. Conclusion

The aerodynamic heat generation and transport mechanisms are investigated in STBLIs generated by a 30° compression ramp at a *Ma* of 5 for a cold wall condition based on theoretical analysis and DNS results. The present DNS results are carefully validated and basically agree with the public hypersonic data. Therefore, the DNS can be regarded as a reliable DNS database that provides detailed information and underlying insights of hypersonic STBLIs. The main conclusions of the paper can be summarized as follows.

(1) The sharp increase of wall heat transfer in the STBLI can be attributed to the boundary layer compression caused by the shock wave and the convection transport enhancement caused by the density increase. Quantitatively, a prediction correlation of wall heat flux is proposed, which includes pressure ratios together with *Ma* and wall temperatures, and reduces the relative error from 72 % to 35 % compared with the canonical Q-P theory. The present correlation can be applied to a wider range of *Ma*, which is proved accurate by some representative data including the present DNS.

(2) Based on the DNS results, the aerodynamic heat generation and transport mechanisms are revealed in the separation, recirculation and reattachment zones in the STBLI. The sharp increase of heat transfer in the interaction region is caused

by the massive generation of compression aerodynamic heat and the enhancement of turbulent dissipation heat accompanied by the enhancement of turbulent heat transport. In addition, the following peak wall heat flux around the reattachment point is due to local oblique impingement compression that results in continuous aerodynamic heating. The turbulent dissipation and transport enhancement are attributed to the enhancement of near-wall turbulent vortices during the interaction. Besides, the generation and transport of compression aerodynamic heat reveal the underlying mechanism of the strong correlation between the peak heat flux ratios and the pressure ratios.

This work can inspire some effective approaches to tackle the serious aerodynamic heating problems in hypersonic STBLIs, including weakening the compression aerodynamic heat generation, inhibiting the heat transport to the near-wall region and reducing turbulence in the recirculation zone. Moreover, it would be interesting to apply the aerodynamic heating analyses and observations made for the 2-D STBLI to swept interactions and more complex 3-D interactions.

Acknowledgements. We thank Prof. Li X.-L. for providing the open source code.

Funding. The study is financially supported by Tsinghua University Initiative Scientific Research Program.

Declaration of interests. The authors report no conflict of interest.

Author ORCID.
Zhenyuan Tang https://orcid.org/0000-0001-7008-3911.

References

Adler, M.C. & Gaitonde, D.V. 2019 Flow similarity in strong swept-shock/turbulent-boundary-layer interactions. *AIAA J.* **57** (4), 1–15.

Andreopoulos, Y., Agui, J.H. & Briassulis, G. 1987 Some new aspects of the shock-wave boundary layer interaction. *J. Fluid Mech.* **180**, 405–428.

Andreopoulos, Y., Agui, J.H. & Briassulis, G. 2000 Shock wave-turbulence interactions. *Annu. Rev. Fluid Mech.* **32** (1), 309–345.

Babinsky, H. & Harvey, J.K. 2011 *Shock Wave-Boundary-Layer Interactions*. Cambridge University Press.

Back, L.H. & Cuffel, R.F. 1970 Changes in heat transfer from turbulent boundary layers interacting with shock waves and expansion waves. *AIAA J.* **8** (10), 1871–1873.

Bernardini, M., Asproulias, I., Larsson, J., Pirozzoli, S. & Grasso, F. 2016 Heat transfer and wall temperature effects in shock wave turbulent boundary layer interactions. *Phys. Rev. Fluids* **1**, 084403.

Bhagwandin, V.A., Helm, C.M. & Martin, P. 2019 Shock wave-turbulent boundary layer interactions in separated compression corners at Mach 10. In *AIAA Scitech 2019 Forum*, p. 1129.

Bookey, P., Wyckham, C., Smits, A. & Martin, P. 2005 New experimental data of STBLI at DNS/LES accessible Reynolds numbers. In *43rd AIAA Aerospace Sciences Meeting and Exhibit*, p. 309.

Brown, G.L. & Roshco, A. 1974 On density effects and large structure in turbulent mixing layers. *J. Fluid Mech.* **64**, 775–816.

Cebeci, T. 2012 *Analysis of Turbulent Boundary Layers*. Elsevier.

Chu, Y.-B., Zhuang, Y.-Q. & Lu, X.-Y. 2013 Effect of wall temperature on hypersonic turbulent boundary layer. *J. Turbul.* **14** (12), 37–57.

Clemens, N.T. & Narayanaswamy, V. 2014 Low-frequency unsteadiness of shock wave turbulent boundary layer interactions. *Annu. Rev. Fluid Mech.* **46**, 469–492.

Coleman, G.T. & Stollery, J.L. 1972 Heat transfer from hypersonic turbulent flow at a wedge compression corner. *J. Fluid Mech.* **56** (4), 741–752.

Delery, J. & Coet, M.-C. 1991 Experiments on shock-wave boundary-layer interactions produced by two-dimensional ramps and three-dimensional obstacles. In *Hypersonic Flows for Reentry Problems: Volume II: Test Cases—Experiments and Computations Proceedings of a Workshop Held in Antibes, France, 22–25 January 1990*, pp. 97–128. Springer.

DOLLING, D.S. 2001 Fifty years of shock-wave boundary-layer interaction research: what next? *AIAA J.* **39** (8), 1517–1531.

VAN DRIEST, E.R. 1956 *The Problem of Aerodynamic Heating*. Institute of the Aeronautical Sciences.

DUAN, L., BEEKMAN, I. & MARTIN, M.P. 2010 Direct numerical simulation of hypersonic turbulent boundary layers. Part 2. Effect of wall temperature. *J. Fluid Mech.* **655**, 419–445.

DUAN, L., BEEKMAN, I. & MARTIN, M.P. 2011 Direct numerical simulation of hypersonic turbulent boundary layers. Part 3. Effect of Mach number. *J. Fluid Mech.* **672**, 245–267.

ECKERT, E.R.G. 1955 Engineering relations for friction and heat transfer to surfaces in high velocity flow. *J. Aeronaut. Sci.* **22** (8), 585–587.

ECKERT, E.R.G. 1960 *Survey of Boundary Layer Heat Transfer at High Velocities and High Temperatures*, vol. 59. Wright Air Development Center.

ERENGIL, M.E. & DOLLING, D.S. 1991 Unsteady wave structure near separation in a Mach 5 compression ramp interaction. *AIAA J.* **29** (5), 728–735.

ERENGIL, M.E. & DOLLING, D.S. 1993 Physical causes of separation shock unsteadiness in shock wave turbulent boundary layer interactions. In *24th AIAA Fluid Dynamics Conference, Orlando, FL*, pp. 1993–3134.

FAN, X.-H., TANG, Z.-G., WANG, G. & YANG, Y.-G. 2022 Review of low-frequency unsteadiness in shock wave turbulent boundary layer interaction. *Acta Aeronaut. Astronaut. Sin.* **43**, 9–29.

FANG, J., ZHELTOVODOV, A.A., YAO, Y.-F., MOULINEC, C. & EMERSON, D.R. 2020 On the turbulence amplification in shock-wave/turbulent boundary layer interaction. *J. Fluid Mech.* **897**, A32.

FU, D.-X., MA, Y.-W. & LI, X.-L. 2010 *Direct Numerical Simulation of Compressible Turbulence*. China Science Press.

GAITONDE, D.V. 2015 Progress in shock wave/boundary layer interactions. *Prog. Aerosp. Sci.* **72**, 80–99.

GANAPATHISUBRAMANI, B., CLEMENN, N.T. & DOLLING, D.S. 2007 Effects of upstream boundary layer on the unsteadiness of shock-induced separation. *J. Fluid Mech.* **585**, 369–94.

GAVIGLIO, J. 1987 Reynolds analogies and experimental study of heat transfer in the supersonic boundary layer. *Intl J. Heat Mass Transfer* **30** (5), 911–926.

GEORGIADIS, N.J., RIZZETTA, D.P. & FUREBY, C. 2010 Large-eddy simulation: current capabilities, recommended practices, and future research. *AIAA J.* **48** (8), 1772–1784.

HAYASHI, M., ASO, S. & TAN, A. 1989 Fluctuation of heat transfer in shock wave turbulent boundary layer interaction. *AIAA J.* **27** (4), 399–404.

HAYASHI, M., SAKURAI, A. & ASO, S. 1986 Measurement of heat-transfer coefficients in shock wave-turbulent boundary layer interaction regions with a multi-layered thin film heat transfer gauge. *Tech. Rep.* NASA.

HELM, C.M. & MARTÍN, M.P. 2022 Large eddy simulation of two separated hypersonic shock/turbulent boundary layer interactions. *Phys. Rev. Fluids* **7** (7), 074601.

HOLDEN, M.S. 1972 Shock wave-turbulent boundary layer interaction in hypersonic flow. In *10th Aerospace Sciences Meeting*, p. 74.

HOLDEN, M.S. 1977 Shock wave-turbulent boundary layer interaction in hypersonic flow. In *15th Aerospace Sciences Meeting*, p. 45.

HONG, Y.-T., LI, Z.-F. & YANG, J.-M. 2021 Scaling of interaction lengths for hypersonic shock wave turbulent boundary layer interactions. *Chin. J. Aeronaut.* **34** (5), 504–509.

HUANG, J.-J., LIAN, D. & CHOUDHARI, M.M. 2022 Direct numerical simulation of hypersonic turbulent boundary layers: effect of spatial evolution and Reynolds number. *J. Fluid Mech.* **937**, A3.

HUANG, P.-G., COLEMAN, G.N. & BRADSHAW, P. 1995 Compressible turbulent channel flows: DNS results and modelling. *J. Fluid Mech.* **305**, 185–218.

HUMBLE, R.A., ELSINGA, G.E., SCARANO, F. & VAN OUDHEUSDE, B.W. 2009 Three-dimensional instantaneous structure of a shock wave/turbulent boundary layer interaction. *J. Fluid Mech.* **622**, 33–62.

HUNG, F. & BARNETT, D. 1973 Shockwave-boundary layer interference heating analysis. In *11th Aerospace Sciences Meeting*, p. 237.

JAMESON, A., SCHMIDT, W. & TURKEL, E. 1981 Numerical solutions of the euler equations by finite volume methods using Runge–Kutta time stepping. In *14th Fluid and Plasma Dynamics Conference, Palo Alto, CA, USA*.

JAUNET, V., DEBIEVE, J.F. & DUPONT, P. 2014 Length scales and time scales of a heated shock-wave/boundary-layer interaction. *AIAA J.* **52** (11), 2524–2532.

LEVIN, V. & FABISH, T.J. 1962 Thermal effects of shock wave turbulent boundary layer interaction at Mach numbers 3 and 5. *Tech. Rep.* North American Aviation.

LI, S.-X. 2007 *Complex Flows Dominated by Shock Waves and Boundary Layers*. China Science Press.

LI, X.-L., FU, D.-X., MA, Y.-W. & LIANG, X. 2010 Direct numerical simulation of shock wave turbulent boundary layer interaction. *Sci. Sin.* **40**, 791–799.

LIANG, X., LI, X.-L., FU, D.-X. & MA, Y.-W. 2012 DNS and analysis of a spatially evolving hypersonic turbulent boundary layer over a flat plate at Mach 8. *Sci. Sin.* **42**, 82–293.

LONGO, J.M. 2003 Aerothermodynamics – a critical review at DLR. *Aerosp. Sci. Technol.* **7** (6), 429–438.

MA, C.-L. & LIU, J.-Y. 2023 Effect of grid strategy on numerical simulation results of aerothermal heating loads over hypersonic blunt bodies. *Acta Aeronaut. Astronaut. Sin.* **44** (05), 73–86.

MAGNAN, J.D. & SPURLIN, C.J. 1966 Investigation of flow field interference caused by shock impingement on a flat plate at Mach numbers of 6, 8 and 10. *Tech. Rep.* Arnold Engineering Development Center, Arnold Air Force Base.

MARKARIAN, C.F. 1968 Heat transfer in shock wave-boundary layer interaction regions. *Tech. Rep.* Naval Weapons Center.

MORKOVIN, M.V. 1962 Effects of compressibility on turbulent flows. *Méc. Turbul.* **367** (380), 26.

MURRAY, N., HILLIER, R. & WILLIAMS, S. 2013 Experimental investigation of axisymmetric hypersonic shock-wave/turbulent-boundary-layer interactions. *J. Fluid Mech.* **714**, 152–189.

PADMANABHAN, S., MALDONADO, J.C., THREADGILL, J.A. & LITTLE, J.C. 2021 Experimental study of swept impinging oblique shock/boundary-layer interactions. *AIAA J.* **59** (1), 140–149.

PIPONNIAU, S., DUSSAUGE, J.P., DEBIEVE, J.F. & DUPONT, P. 2009 A simple model for low-frequency unsteadiness in shock-induced separation. *J. Fluid Mech.* **629**, 87–108.

PIROZZOLI, S., GRASSO, F. & GATSKI, T.B. 2004 Direct numerical simulation and analysis of a spatially evolving supersonic turbulent boundary layer at $M = 2.25$. *Phys. Fluids* **16** (3), 530–545.

PRIEBE, S. & MARTIN, M.P. 2012 Low-frequency unsteadiness in shock wave-turbulent boundary layer interaction. *J. Fluid Mech.* **699**, 1–49.

PRIEBE, S. & MARTÍN, M.P. 2021 Turbulence in a hypersonic compression ramp flow. *Phys. Rev. Fluids* **6** (3), 034601.

QU, Z.-H., LIU, W., ZENG, M. & LIU, J. 2001 *Hypersonic Aerodynamics*. National University of Defense Technology Press.

ROSHCO, A. 1976 Structure of turbulent shear flows: a new look. *AIAA J.* **14**, 1349–1357.

RUBESIN, M.W. 1990 Extra compressibility terms for Favre-averaged two-equation models of inhomogeneous turbulent flows. *Tech. Rep.* NASA.

SAYANO, S., BAUSCH, H.P. & DONNELLY, R.J. 1962 Aerodynamic heating due to shock impingement on a flat plate. *Tech. Rep.* McDonnell-Douglas Aircraft Co..

SCHREYER, A.M., SAHOO, D., WILLIAMS, O.J.H. & SMITS, A.J. 2018 Experimental investigation of two hypersonic shock/turbulent boundary-layer interactions. *AIAA J.* **56** (12), 4830–4844.

SCHÜLEIN, E. 2006 Skin friction and heat flux measurements in shock/boundary layer interaction flows. *AIAA J.* **44** (8), 1732–1741.

SCHÜLEIN, E., KROGMANN, P. & STANEWSKY, E. 1996 Documentation of two-dimensional impinging shock/turbulent boundary layer interaction flows. *Tech. Rep.* DLR, German Aerospace Research Center.

SILLERO, J.A., JIMENEZ, J. & MOSER, R.D. 2013 One-point statistics for turbulent wall-bounded flows at Reynolds numbers up to delta+ 2000. *Phys. Fluids* **25** (10), 133–166.

SOUVEREIN, L.J., BAKKER, P.G. & DUPONT, P. 2013 A scaling analysis for turbulent shock-wave boundary-layer interactions. *J. Fluid Mech.* **714**, 505–535.

SPAID, F.W. & FRISHETT, J.C. 1972 Incipient separation of a supersonic, turbulent boundary layer, including effect of heat transfer. *AIAA J.* **10** (7), 915–922.

SPALART, P.R. 1988 Direct simulation of a turbulent boundary layer up to $R_\theta = 1410$. *J. Fluid Mech.* **187**, 61–98.

SUN, D., GUO, Q.-L., YUAN, X.-X., ZHANG, H.-Y., LI, C. & LIU, P.-X. 2021 A decomposition formula for the wall heat flux of a compressible boundary layer. *Adv. Aerodyn.* **3** (1), 33.

THOMAS, F.O., PUTNAM, C.M. & CHU, H.-C. 1994 On the mechanism of unsteady shock oscillation in shock wave/turbulent boundary layer interactions. *Exp. Fluids* **18**, 69–81.

TONG, F.-L., DONG, S.-W., LAI, J., YUAN, X.-X. & LI, X.-X. 2022*a* Wall shear stress and wall heat flux in a supersonic turbulent boundary layer. *Phys. Fluids* **34** (1), 015127.

TONG, F.-L., DUAN, J.-Y. & LI, X.-L. 2021 Shock wave and turbulent boundary layer interaction in a double compression ramp. *Comput. Fluids* **229**, 105087.

TONG, F.-L., LI, X., YU, C.-P. & LI, X.-L. 2018 Direct numerical simulation of hypersonic shock wave and turbulent boundary layer interactions. *Chin. J. Theor. Appl. Mech.* **50** (2), 197–208.

TONG, F.-L., YUAN, X.-X., LAI, J., DUAN, J.-Y., SUN, D. & DONG, S.-W. 2022*b* Wall heat flux in a supersonic shock wave turbulent boundary layer interaction. *Phys. Fluids* **34** (6), 065104.

VANSTONE & CLEMENS 2019 Proper orthogonal decomposition analysis of swept-ramp shockwave/boundary-layer unsteadiness at Mach 2. *AIAA J.* **57** (8), 3395–3409.

VOLPIANI, P.S., BERNARDINI, M. & LARSSON, J. 2018 Effects of a nonadiabatic wall on supersonic shock/boundary-layer interactions. *Phys. Rev. Fluids* **3** (1), 083401.

VOLPIANI, P.S., BERNARDINI, M. & LARSSON, J. 2020 Effects of a nonadiabatic wall on hypersonic shock/boundary-layer interactions. *Phys. Rev. Fluids* **5** (1), 014602.

WAGNER, A., SCHRAMM, J.M., HANNEMANN, K., WHITSIDE, R. & HICKEY, J.-P. 2017 Hypersonic shock wave boundary layer interaction studies on a flat plate at elevated surface temperature. In *International Conference on RailNewcastle Talks*, pp. 231–243.

WALZ, A. & OSER, H.J. 1969 *Boundary Layers of Flow and Temperature*. M.I.T. Press.

WENZEL, C., SELENT, B., KLOKER, M. & RIST, U. 2018 DNS of compressible turbulent boundary layers and assessment of data/scaling-law quality. *J. Fluid Mech.* **842**, 428–468.

WHITE, F.M. & MAJDALANI, J. 2006 *Viscous Fluid Flow*, vol. 3. McGraw-Hill Higher Education New York.

WU, M. & MARTIN, M.P. 2008 Analysis of shock motion in shockwave and turbulent boundary layer interaction using direct numerical simulation data. *J. Fluid Mech.* **594**, 71–83.

ZHANG, C., DUAN, L. & CHOUDHARI, M.M. 2018 Direct numerical simulation database for supersonic and hypersonic turbulent boundary layers. *AIAA J.* **56** (11), 4297–4311.

ZHANG, Y.-S., BI, W.-T., HUSSAIN, F. & SHE, Z.-S. 2014 A generalized Reynolds analogy for compressible wall-bounded turbulent flows. *J. Fluid Mech.* **739**, 392–420.

ZHANG, Z.-S., CIU, G.-X., XU, C.-X. & HUANG, W.-X. 2017 *Theory and Modeling of Turbulence*. Tsinghua University Press.

ZHU, X.-K., YU, C.-P., TONG, F.-L. & LI, X.-L. 2017 Numerical study on wall temperature effects on shock wave turbulent boundary-layer interaction. *AIAA J.* **55** (1), 131–140.

ZUO, F.-Y. 2023 Hypersonic shock wave/turbulent boundary layer interaction over a compression ramp. *AIAA J.* **61** (4), 1579–1595.

ZUO, F.-Y., WEI, J.-R., HU, S.-L. & PIROZZOLI, S. 2022 Effects of wall temperature on hypersonic impinging shock-wave/turbulent-boundary-layer interactions. *AIAA J.* **60** (9), 5109–5122.